https://doi.org/10.5194/egusphere-2026-4587
Preprint. Discussion started: 3 August 2026

A two-way street across three oceans: observed Madden Julian Oscillation – oceanic Kelvin wave coupling in boreal winter.

Fernando Belinchón[1,2], Elsa Mohino[1], and Irene Polo[1]

[1]Departamento de Física de la Tierra y Astrofísica, Universidad Complutense de Madrid, Madrid, Spain.
[2]Modelling Area– Department of Development and Applications, State Meteorological Agency (AEMET), 28040 Madrid, Spain.

Correspondence: Fernando Belinchón (ferbelin@ucm.es), Elsa Mohino (emohino@ucm.es), and Irene Polo (ipolo@fis.ucm.es)

Abstract. Air–sea coupling associated with the Madden–Julian Oscillation (MJO) plays a central role in subseasonal variability and prediction, yet its two-way interaction with oceanic Kelvin waves (KWs) across the tropical basins remains insufficiently constrained. Here we assess both the impact of KWs on MJO evolution through sea surface temperature (SST) changes, and the characteristics of MJO events that lead to KW generation and propagation in the Indian, Pacific and Atlantic oceans during boreal winter. In a novel way, we combine MJO index with independent KW indices for each basin, identifying regimes of enhanced and suppressed KW activity and quantify the MJO-associated forcing and the strength of air–sea feedbacks.

The capacity of the MJO to force KWs varies markedly across basins, ranging from a minimum of 38% of MJO events generating KWs in the Pacific, to 16.8% in the Indian Ocean and to 9.4% in the Atlantic. In all three basins, KW generation is favored when MJO events display strong, coherent equatorial low-level zonal wind anomalies and organized eastward-propagating convection, which force a continuous sea surface height (SSH) signal with a clear KW structure. In the Pacific, the resulting thermocline displacements propagate coherently across the basin and reach the surface in the far east, where they drive SST changes primarily through vertical advection and meridional geostrophic advection. In the Indian ocean, wind anomalies over the central basin force an SSH signal that intensifies toward the east and evolves into a coherent equatorially trapped structure, a process that appears to be modulated by a preceding oceanic Rossby wave. In the Atlantic, KW generation requires coherent westerly wind stress anomalies along the equator near the South American coast and is further favored by an atmospheric KW originating over the Indo-Pacific that promotes convection in the western basin. Conversely, events that fail to generate KWs share a common signature across basins: weaker or off-equatorial wind forcing and SSH anomalies that lose coherence before reaching the eastern side of each basin. In the Atlantic, this decoupled regime leaves convective anomalies concentrated over the eastern basin and the Guinea Dome, largely detached from the equatorial ocean response.

From the oceanic perspective, a substantial fraction of KWs in each basin is associated with the MJO, and their presence systematically strengthens ocean–atmosphere coupling. Under enhanced KW activity, ocean dynamics govern SST tendencies in both the Pacific and the Atlantic. In the Pacific, subsurface adjustments sustain SST anomalies and support the eastward advance of the MJO even where atmospheric forcing weakens. In the Indian Ocean, by contrast, surface heat fluxes dominate SST variability. In periods of suppressed KW activity, surface fluxes dominate SST variability across all three basins, except in the eastern Pacific, where local processes such as surface current convergence dominate instead. These results establish the

https://doi.org/10.5194/egusphere-2026-4587
Preprint. Discussion started: 3 August 2026

MJO–KW relationship as a genuinely two-way interaction, with implications for subseasonal prediction in all three tropical basins. It is necessary to study the interaction with the MJO in each basin separately or in greater detail, given the unique characteristics of each basin and its modes of variability.

1 Introduction

The Madden-Julian oscillation (MJO) constitutes the dominant mode of climate variability in the tropics (Madden and Julian, 1971; Zhou and Miller, 2005). Initially identified through spectral analysis of surface pressure and upper-air data from tropical stations (Madden and Julian, 1972), the MJO is characterized by a large-scale, eastward-propagating envelope of enhanced and suppressed convection, with a typical period of 30 to 70 days (DeMott et al., 2015). Since its discovery, the MJO has become a central element in the study of tropical dynamics, due to its extensive influence on monsoon variability and tropical cyclone activity (Lin et al., 2009; Vitart and Molteni, 2010; Zhang, 2013). Subseasonal to seasonal forecasting systems that accurately capture the MJO's initiation and propagation tend to exhibit enhanced performance in simulating tropical convection and its teleconnections (Kim et al., 2016; Wang et al., 2014).

The MJO is primarily diagnosed using anomalies in zonal winds at 850 hPa (u850) and 250 hPa (u250), together with outgoing longwave radiation (OLR), which serves as a proxy for deep convective activity (Wheeler and Hendon, 2004). While the strongest MJO signals are typically observed in the Indian ocean and the western Pacific, the phenomenon exerts influence across the entire tropical belt, including the Atlantic basin (Cassou, 2008; Grimm, 2019). This broad spatial footprint highlights the relevance of studying the MJO from a multi-basin perspective.

The MJO interacts strongly with the upper ocean (Klingaman and Woolnough, 2014). Wind stress, radiative forcing, and precipitation anomalies associated with the MJO modify the ocean surface and subsurface through processes such as heat flux variability, mixed-layer adjustment, and freshwater fluxes (DeMott et al., 2015). In addition to this atmospheric forcing of the ocean, feedbacks from the ocean surface—such as sea surface temperature (SST) anomalies and mixed-layer dynamics—can modulate the intensity, coherence, and propagation characteristics of the MJO itself (Drushka et al., 2014; DeMott et al., 2015; Klingaman and Woolnough, 2014). These interactions lead to anomalies in SST, upper-ocean stratification, and the generation of equatorially trapped waves, most notably Kelvin waves (KWs) (Rydbeck et al., 2019; Webber et al., 2010). These oceanic waves, derived as solutions to the linear shallow water equations formulated by Matsuno (1966), propagate eastward along the equator and exhibit a meridional decay in amplitude consistent with a Gaussian structure (Fedorov and Brown, 2009).

In the Indo-Pacific region, such air–sea interactions are well documented and play a key role in intraseasonal oceanic variability. In the Indian ocean, intraseasonal wind stress anomalies generate equatorial KWs and Rossby waves that propagate across the basin and influence thermocline depth, upper-ocean stratification, and SST variability (Webber et al., 2010; Moum et al., 2016; Liu et al., 2021). Further east, in the Pacific ocean, these coupled ocean–atmosphere processes contribute significantly to intraseasonal variability and to the development of interannual phenomena such El Niño (Kessler et al., 1995; Slingo et al., 1999; McPhaden and Yu, 1999; Hendon et al., 1999). Strong MJO events can initiate westerly wind bursts in the western Pacific, leading to the generation of downwelling KWs that propagate eastward along the equator, deepening the thermocline and contributing to the onset of El Niño events (Matthews and Kiladis, 1999; Lee et al., 2019). These MJO-related westerly wind bursts have been identified as important triggers for downwelling KWs that propagate into the central and eastern Pacific, modifying upper-ocean stratification and preconditioning the ocean for the development of subsequent SST anomalies (Kessler et al., 1995; Liang and Fedorov, 2021; Seo and Xue, 2005; Zhang and Gottschalck, 2002).

Although the Indo-Pacific has received the most attention in MJO–ocean interaction studies, recent work has increasingly demonstrated that the Atlantic ocean also exhibits a measurable response to MJO variability (Lee et al., 2023; Vera et al., 2018). The Atlantic sector can be influenced by MJO-related signals originating in the Indo-Pacific through zonally propagating atmospheric waves and coherent wind anomalies that impact convection and air–sea interaction in the basin (Janicot et al., 2011). Moreover, MJO-induced wind anomalies over the western Atlantic can generate KWs that propagate eastward and modulate upper-ocean conditions along the equator (Webber et al., 2010). These processes are also linked to variability in the position and intensity of the Intertropical Convergence Zone (ITCZ), regional precipitation patterns, and the modulation of tropical cyclone activity (Alaka and Maloney, 2012; Ventrice et al., 2011).

Aside from air-sea coupling, the MJO has broad impacts. During boreal winter, December to February (DJF), when the MJO is especially active (Zhang and Dong, 2004), enhanced MJO activity in the warm pool has been associated with with a positive phase of the NAO (Lin et al., 2009; Zhou and Miller, 2005). This interaction underscores the MJO's role in driving extratropical climate variability during winter (Cassou, 2008; Seo and Son, 2012). Along the West African coast, intraseasonal SST variability in the tropical Atlantic upwelling regions is shaped by coastal KWs, wind forcing, and vertical mixing, with anomalies in Angola-Benguela linked to pressure patterns associated with the MJO, the St Helena Anticyclone, and the Antarctic Oscillation (Diakhaté et al., 2016). Additionally, the MJO modulates convection and rainfall variability over the Amazon basin and tropical South America on intraseasonal timescales. Through its influence on the South American monsoon system and the South Atlantic Convergence Zone, different MJO phases are associated with changes in precipitation patterns and circulation anomalies across the region, particularly during the austral summer when the monsoon is active (Carvalho et al., 2004; Alvarez et al., 2016; Vera et al., 2018). Observational analyses further show that the evolution of intraseasonal rainfall events in the Amazon basin is coherently related to the phase of the MJO, highlighting its role in modulating precipitation variability across the region (Mayta et al., 2019).

Previous research has struggled to disentangle distinct MJO signals from the oceanic response, due both to the complexity of individual basins and to methodological limitations. Identifying oceanic KWs associated with the MJO has posed persistent challenges in previous literature, although the nature of these challenges varies by region. In the Indian ocean, strong convective activity, intense radiative forcing, and the dominance of Rossby wave signals often obscure the KW signature (Rydbeck et al., 2021; Webber et al., 2010). In contrast, in the Atlantic ocean, the MJO itself is considerably weaker, which limits the strength and clarity of its oceanic imprint and complicates the detection of associated KWs (Webber et al., 2010). In addition, previous studies have investigated the impact of the MJO on the ocean using observational and reanalysis data, detecting anomalous signals at depths of up to 2,000 m, predominantly in the Pacific, associated with the vertical propagation of the surface-forced signal (Matthews et al., 2010; Robbins et al., 2025). These studies reveal a characteristic tilt in the anomalous potential density, salinity, and temperature fields, consistent with a KW forced by MJO-associated zonal wind anomalies. Nevertheless, the rela-

https://doi.org/10.5194/egusphere-2026-4587
Preprint. Discussion started: 3 August 2026

tionship between the vertical structure of the KW response and the surface forcing exerted by the MJO remains insufficiently understood. To address these challenges, the present work adopts a purely observational approach and examines the interaction between the MJO and equatorial KWs by introducing a novel methodolgy based on the construction of a MJO-KW congingency table with the aim of determining whether ocean-atmosphere coupling plays a significant role in the manifestation and propagation of the MJO. It combines the Wheeler and Hendon MJO index (Wheeler and Hendon, 2004) with a KW index derived from SSH anomalies (Rydbeck et al., 2019) into a 2-D structure that allows us to address the following key scientific questions: do all MJO events give rise to equatorial KWs? If not, what distinguishes those MJO events that generate KWs from those that do not? Furthermore, are all equatorial KWs associated with MJO propagation? What role does the presence of KWs play in facilitating or modulating the eastward propagation of the MJO across ocean basins and what are the oceanic responses to the different forcing mechanisms associated with the MJO?

This multi-basin approach provides a unified view of MJO–KW interactions, contributing to an improved understanding of intraseasonal ocean–atmosphere coupling and its role in modulating tropical variability. The structure of the paper is as follows: Section 2 describes the data sets and methodological framework. Section 3 presents the main results. Section 4 discusses the implications of these findings, and Section 5 concludes with a summary and future research directions.

2 Data

To capture the MJO signal, we employ a suite of atmospheric and oceanic variables. Dynamical fields are represented by u850 and u250, while convective activity is characterized using OLR. The zonal wind data are obtained from the ERA5 reanalysis, produced by the European Centre for Medium-Range Weather Forecasts (ECMWF) (Soci et al., 2024), which provides global fields at a horizontal resolution of approximately 31 km, with an hourly temporal resolution and a temporal coverage spanning from 1940 to 2022. Hourly ERA5 wind data are regridded to a 1º × 1º spatial grid and averaged to daily means for computational efficiency and dataset consistency. OLR data are taken from the NOAA interpolated OLR product (Kalnay et al., 1996), which provides data at a spatial resolution of 2.5° × 2.5°, with daily temporal frequency and coverage from 1979 to the present. This dataset is used at its original resolution.

To capture equatorial KWs, we incorporate sea surface height (SSH) anomalies from satellite altimetry products provided by the Copernicus Marine Environment Monitoring Service (CMEMS), specifically the GLORYS12V1 global ocean reanalysis (Lellouche et al., 2021). This product offers daily fields at a native horizontal resolution of 1/12° (∼8 km) and 50 vertical levels, spanning from January 1993 to the present. GLORYS12V1 is based on the NEMO ocean model, driven by ECMWF surface reanalyses (ERA-Interim and ERA5 in recent years), and assimilates a range of observational data—including along-track sea level anomalies, satellite-derived SST, sea ice concentration, and in situ temperature and salinity profiles—using a reduced-order Kalman filter and a 3D-VAR bias correction scheme. The SSH fields are interpolated to a 1° × 1° grid to ensure consistency with other variables, and we focus on the period 1994–2021 for analysis.

https://doi.org/10.5194/egusphere-2026-4587
Preprint. Discussion started: 3 August 2026

Beyond the primary MJO indicators, we examine the response of the surface energy budget to MJO activity using additional surface flux variables. From ERA5, we use surface wind stress, surface net solar and longwave radiation, sensible heat flux, and latent heat flux. These fields are available at hourly temporal resolution and are regridded to a 1° × 1° grid.

Complementary oceanic variables are also obtained from the GLORYS12V1 product, including SST, surface ocean currents, and vertical profiles of ocean potential temperature. All fields are provided at daily temporal resolution and regridded to a common 1° × 1° grid. The SST and surface current fields are extracted across the tropical belt (15°S–15°N), encompassing all longitudes. We denote ∂_tSST as the daily rate of change in SST, defined as the difference between consecutive days divided by one day. Additionally, vertical profiles of potential temperature are sampled along the equator at latitudes -0.25°, 0°, and 0.25°, from the surface down to 272 m depth. This configuration allows for a detailed examination of the coupled atmosphere–ocean dynamics associated with MJO propagation and the potential role of KW activity in different ocean basins.

3 Metodology

We focus on the boreal winter season, defined here as the DJF months, during which the MJO exhibits its highest amplitude and strongest coherence, particularly over the eastern Indian ocean and the western Pacific (Lafleur et al., 2015). The analysis is restricted to the tropical belt between 15°S and 15°N across all longitudes, where the MJO signal is most active. To identify and characterize MJO events, we follow the methodology introduced by Wheeler and Hendon (2004), which constructs a MJO index based on multivariate empirical orthogonal function (EOF) analysis. The input fields used for this analysis are OLR, u850 and u250, as described in Section 2. These variables are averaged meridionally over the 15°S–15°N band. Prior to the EOF analysis, all variables undergo several preprocessing steps. First, we remove the seasonal cycle by subtracting the mean and the first three annual harmonics at each grid point. Next, a 2nd-order Butterworth band-pass filter (Butterworth, 1930) is applied to isolate the intraseasonal variability within the 20–90-day period. The dataset is then restricted to the DJF months and the resulting anomalies are standardized by dividing each field by its standard deviation calculated over the DJF season at each grid point. The resulting covariance matrix is subjected to EOF decomposition. We retain the first two leading EOFs, which capture the coherent spatiotemporal structure of the MJO. These two modes are found to be significantly correlated with each other in quadrature, with the maximum correlation occurring at a lag of 10 days (not shown) with an eastward propagation, as expected for the MJO (Wheeler and Hendon, 2004). This property supports the interpretation of these two EOFs as a pair representing a single propagating mode. Their associated principal components (PCs) define a two-dimensional phase space in which the MJO evolution can be tracked.

Figure 1a illustrates the projection of each DJF day between 1994 and 2021 onto the principal component phase space. Red points highlight the 2020–2021 period with temporal progression following a counterclockwise trajectory. Each day is assigned a phase label, 1 through 8, according to its angular position in this space, provided the amplitude, i.e., distance from the origin, exceeds one standard deviation. Days within the unit circle are classified as "no MJO" days and are excluded from the phase-based compositing. We refer to the distribution of days across the eight phases and the no MJO region collectively as the MJO index. Figure 1b presents the normalized spatial patterns of the first and second EOFs of OLR, u850 and u250. In

https://doi.org/10.5194/egusphere-2026-4587
Preprint. Discussion started: 3 August 2026

the first EOF (blue lines), enhanced convection (negative OLR anomalies) is centered between approximately 60°E and 150°E over the Maritime Continent and western Pacific warm pool. Within this region, low-level westerly wind anomalies (u850) and upper-level easterlies (u250) exhibit an out-of-phase relationship, consistent with the baroclinic structure of the MJO. The second EOF (green lines) displays a quadrature-like structure, with a shift in the convective signal (negative OLR anomalies) toward 120°–180°E. The associated u850 and u250 patterns retain the vertical wind shear characteristic of the MJO, with the peak anomalies also displaced eastward relative to those in EOF1. This spatial shift supports the interpretation of the second EOF as a propagating phase of the MJO, with convection and circulation anomalies evolving coherently across the equatorial belt.

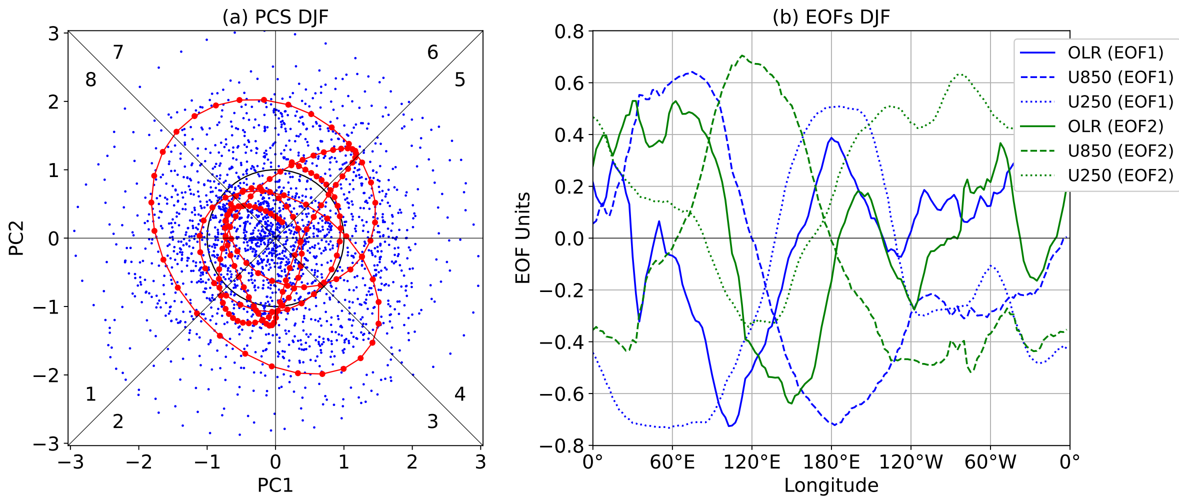

Figure 1. (a) Phase space points for the period 1994–2021 during the months of DJF. The red points correspond to the years 2020–2021. (b) First and second EOFs of OLR (Wm^{-2}) and u850 and u250 (ms^{-1}), averaged over 15°S–15°N and shown as a function of longitude. All fields are standardized.

To isolate the equatorial KW signal, we follow a methodology adapted from Rydbeck et al. (2019), who developed a phase index based on SSH to identify the eastward-propagating component associated with equatorial KWs in the Pacific ocean. We extend their approach to all three tropical ocean basins. As in the MJO analysis, we begin by deseasonalizing the SSH field, removing the annual mean value and its first three harmonics. We then apply a 2nd-order Butterworth band-pass filter to retain variability in the 20–90-day period range. This temporal window was chosen to maintain consistency with the methodology commonly used for the MJO. Furthermore, spectral plots of SSH (not shown) indicate the presence of spectral energy at these frequencies associated with KWs across all three ocean basins. The anomalies are subsequently standardized by dividing by the standard deviation computed over DJF. We define longitudinal windows in each basin to extract the SSH signal, taking into account that KWs are confined near the equator, with a meridional structure that decays approximately as a Gaussian function with latitude. In the Indian ocean, we use longitudes from 50ºE to 95ºE; in the Pacific ocean, from 150ºE to 90ºW; and in the Atlantic ocean, from 44ºW to 9ºE.

https://doi.org/10.5194/egusphere-2026-4587
Preprint. Discussion started: 3 August 2026

For each basin, we compute EOFs of the filtered and standardized SSH anomalies averaged over 2°S–2°N. The first two EOFs and their associated PCs capture the dominant eastward-propagating variability and are used to define the phase and amplitude of the equatorial KW in each basin. As in the MJO methodology, only days with amplitude exceeding one standard deviation in the principal components phase space are retained for compositing. Moreover, The KW index is defined by classifying days into eight phases when the amplitude exceeds one standard deviation in principal component space, plus a suppressed phase for days with lower amplitude. The KW index differs across basins, as distinct longitudinal windows are selected for each region.

To investigate the interaction between equatorial KWs and the MJO in each basin, we assess the co-occurrence of their phases by constructing a contingency table (see Table 1 for the Pacific). Each cell in the table counts the number of days during which a given MJO phase coincides with a particular Kelvin phase. This classification enables us to evaluate whether certain MJO phases are more likely to co-occur with specific KW phases than would be expected by chance.

Next, we performed a chi-squared test of independence (Gorgas García et al., 2011) to evaluate if the MJO and KW indices are statistically related. This test assesses whether the joint occurrences of MJO and KW activity differ significantly from what would be expected under the assumption of independence between the two phenomena. It compares the observed frequencies of days classified by the presence or absence of MJO and KW activity with the corresponding expected frequencies derived from their marginal distributions. A large chi-squared statistic, relative to its theoretical chi-squared distribution, indicates that the discrepancies between observed and expected frequencies are unlikely to have arisen by chance. In the context of a contingency table with I rows and J columns, the chi-squared test statistic is defined as

$$\chi^2_\nu = \sum_{i=1}^{I}\sum_{j=1}^{J}\frac{(o_{ij}-e_{ij})^2}{e_{ij}}, \tag{1}$$

where o_{ij} denotes the observed frequency in cell (i,j), and e_{ij} is the expected frequency under the null hypothesis of independence between the two categorical variables. The expected frequencies are computed as

$$e_{ij} = \frac{(\text{row total})_i\,(\text{column total})_j}{\text{grand total}}, \tag{2}$$

reflecting the assumption that, under independence, the joint probability of belonging to row i and column j factorizes into the product of the corresponding marginal probabilities. If the value of χ^2_ν in Eq. (1) is large compared with the chi-squared distribution with $\nu = (I-1)(J-1)$ degrees of freedom, or equivalently, if the associated p-value is sufficiently small, the null hypothesis is rejected. This outcome implies that the observed deviations between o_{ij} and e_{ij} are too large to be attributed to random sampling variability, providing statistical evidence for an association between the two categorical variables.

To determine the statistical significance of the observed associations, we adopt an empirical permutation test via a Monte Carlo approach. Specifically, we generate 10,000 surrogate realizations of the MJO index by randomly permuting entire DJF seasons with replacement, thereby preserving the intraseasonal structure and temporal autocorrelation within each season. For each surrogate, we recompute the contingency table while keeping the original KW index fixed. This yields a distribution of expected co-occurrence counts under the null hypothesis of no systematic relationship between MJO and KW phases. To

https://doi.org/10.5194/egusphere-2026-4587
Preprint. Discussion started: 3 August 2026

determine whether the observed co-occurrence frequencies deviate significantly from this null distribution, we conduct a two-tailed test at the 95% confidence level. Specifically, we compare the observed counts to the 2.5th and 97.5th percentiles of the permutation based distribution. Phase combinations falling outside this range are considered statistically significant, indicating that they occur either more or less frequently than expected by chance.

The contingency tables provide the foundation for analyzing the interaction between equatorial KWs, the MJO and their associated processes across the three ocean basins. We adopt two complementary approaches: one based on Hovmöller diagram composites and the other focuses on individual MJO events identified through MJO–KW crossed phases. In the first approach, applied to the Pacific and Indian oceans, we identify contingency table entries that are statistically significant at the 95% confidence level in the upper tail—i.e., combinations in which certain phases of the MJO coincide more frequently than would be expected by chance with certain phases of KW. For these significant entries, we composite Hovmöller diagrams of various atmospheric and oceanic variables to characterize the spatiotemporal structure of the MJO under strong KW interaction. To serve as a baseline for comparison, we also construct Hovmöllers using MJO days classified as occurring under suppressed KW conditions (i.e. when the amplitude of the corresponding KW PCs in the phase space does not exceed 1 standard deviation). The comparison between these two cases allows us to assess how coherent KW activity influences the evolution and structure of the MJO, and conversely, how variations in the MJO—through associated atmospheric variables such as wind stress—modify the oceanic response.

In cases where the number of significant entries is insufficient for constructing robust composites, particularly in the Atlantic and in the Indian ocean, we adopt a second, event based strategy. This method involves selecting one MJO phase that significantly co-occurs with KW activity and another instance of the same MJO phase under suppressed KW conditions. We then identify individual MJO events within each of these two categories and apply lead–lag composite maps to various fields. This approach enables a more detailed temporal assessment of the MJO's behavior under conditions of active versus suppressed KW activity and provides a way to circumvent the limitation arising from the limited number of contingency table entries that show statistically significant positive deviations. Across the different figures in which composites or Hovmöller diagrams are constructed based on phases or events, a Student's t test is applied at the 95% confidence level.

To evaluate the robustness of the results, we repeated the analysis using thermocline depth as an alternative proxy for equatorial KWs (not shown), derived from the vertical structure of potential temperature. The phase relationships obtained were qualitatively consistent with those based on SSH, confirming that the observed associations are not sensitive to the specific variable used to characterize KW activity.

https://doi.org/10.5194/egusphere-2026-4587
Preprint. Discussion started: 3 August 2026

4 Results

4.1 Assessment of MJO Index and KW Indices

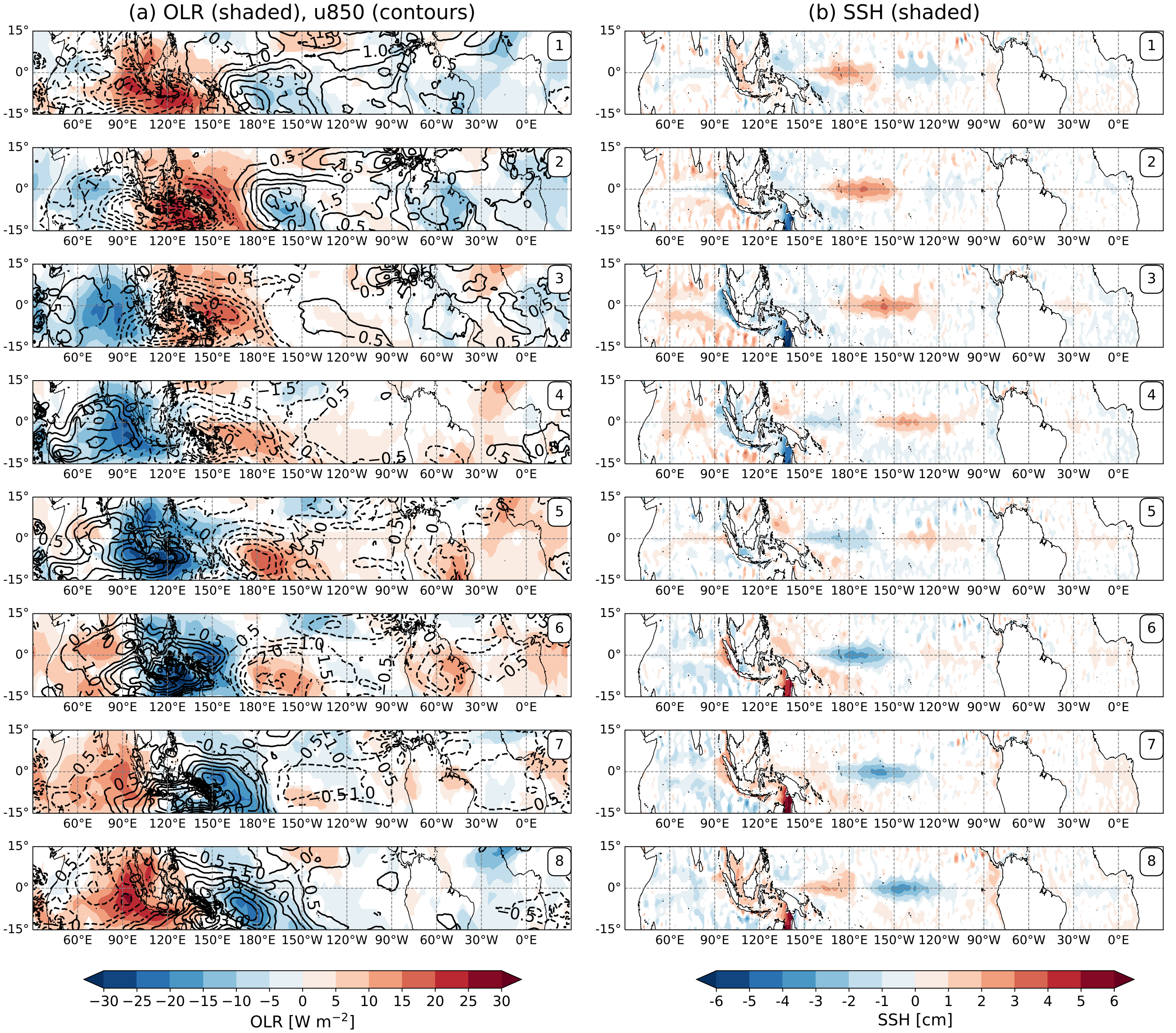

Figure 2. Composite anomalies maps of atmospheric and oceanic fields associated with the MJO: (a) OLR anomalies (shaded in Wm^{-2}) and u850 wind anomalies (contours from –5 to 5 ms^{-1} at 0.5 ms^{-1} intervals) composited by MJO phase; (b) SSH anomalies (shaded in cm) composited by MJO phase. Shaded regions represent only statistically significant anomalies at the 95% confidence level, while contour lines are shown in black for significant values; dashed contours indicate negative values, whereas solid contours denote positive values. The numbers in the upper right corners of the composites indicate the phases of the MJO.

https://doi.org/10.5194/egusphere-2026-4587
Preprint. Discussion started: 3 August 2026

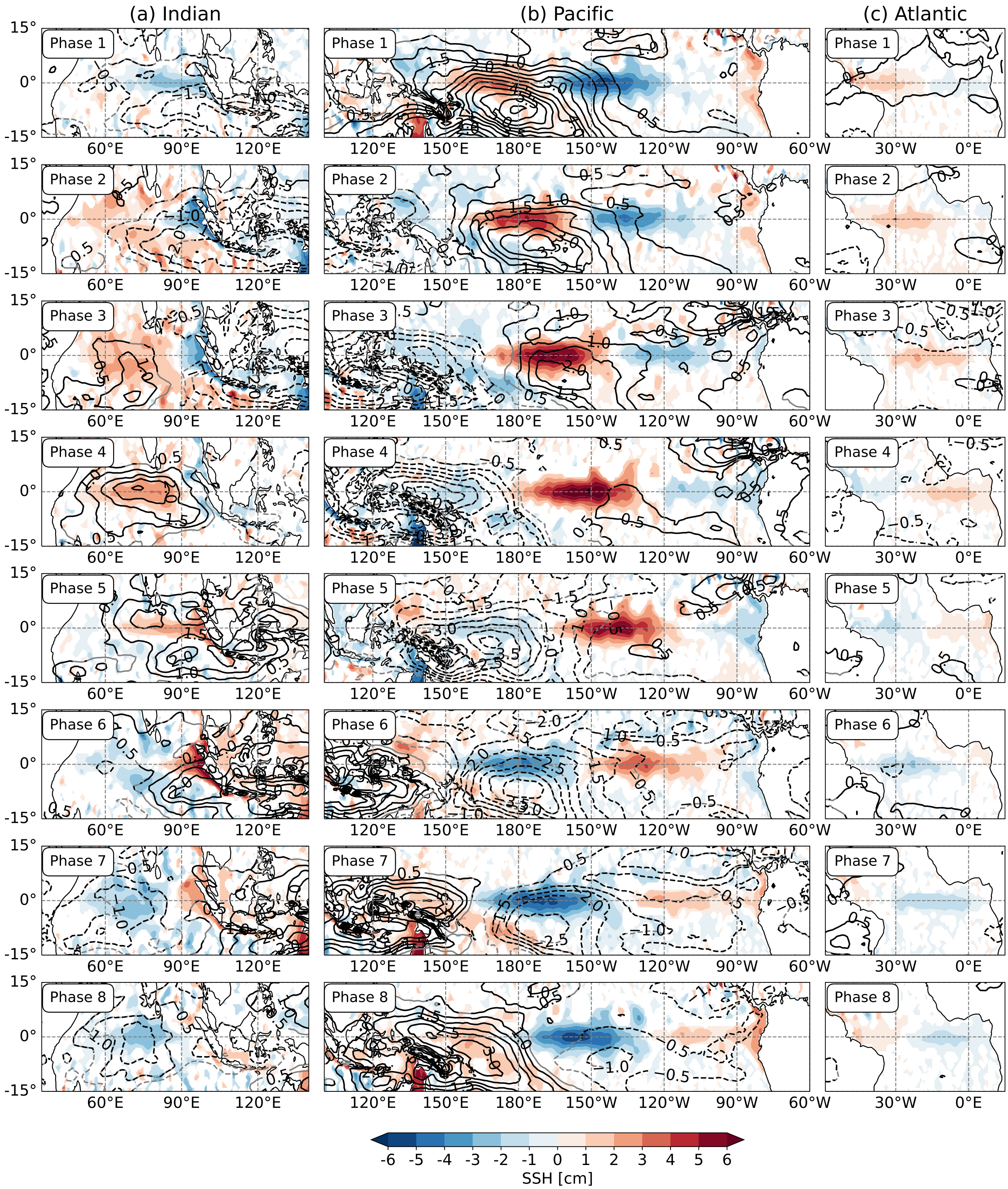

Figure 3. Composite anomalies associated with equatorial KWs across different ocean basins: (a) Indian; (b) Pacific; (c) Atlantic ocean by KW phase defined specifically for each basin. The maps display SSH anomalies (shaded in cm) and u850 wind anomalies (contours from –5 to 5 ms^{-1} at 0.5 ms^{-1} intervals). Shaded regions represent only statistically significant anomalies at the 95 % confidence level, while contour lines are shown in gray for non-significant values and in black for significant values; dashed contours indicate negative values, whereas solid contours denote positive values.

https://doi.org/10.5194/egusphere-2026-4587
Preprint. Discussion started: 3 August 2026

Figure 2a illustrates MJO-related anomalies in OLR and 850-hPa zonal wind across the tropics. The strongest convective signals occur over the Indian ocean, where enhanced convection during Phase 4, marked by negative OLR anomalies, coincides with low-level wind convergence and westerlies up to 2.5 ms^{-1} at 75ºE. This convective center originates in Phase 2 and propagates eastward, crossing the Maritime Continent by Phase 6. Conversely, positive OLR anomalies, indicative of suppressed convection, develop over the central Indian ocean in Phase 6 and advance eastward with easterlies reaching 2.5 ms^{-1} at 75ºE in Phase 8. Over the western Pacific, these anomalies weaken as they progress eastward, while signals in the eastern Pacific and Atlantic remain comparatively weak. In the eastern Pacific, OLR anomalies rarely exceed ± 5 Wm^{-2}, and associated winds are generally below 1.5 ms^{-1}. The Atlantic exhibits stronger OLR anomalies, particularly over Brazil where they exceed 15 Wm^{-2} and in the Guinea Dome region, where values surpass $\pm$ 10 Wm^{-2}, though wind anomalies remain modest (<1 ms^{-1}). Our results are consistent with those presented by Wheeler and Hendon (2004), who analysed OLR and zonal wind anomalies for DJF during the 1979–2001 period. Although we observe anomalies of similar magnitude and sign, their results reveal a phase lag of approximately one phase, with our phases occurring slightly later. Such discrepancies are expected, as phase definitions are empirically derived from data and the analyzed periods differ.

Figure 2b shows the MJO imprint on the upper ocean across the three basins through SSH anomalies. In the Indian ocean, positive SSH anomalies are observed during Phases 2 to 5, while negative anomalies appear during Phases 6 to 1, although the equatorial signal is this basin is very weak. Notably, SSH exhibits positive anomalies on both sides of the equator during Phases 2 to 4, and anomalies of opposite sign during Phases 6 to 8, which may indicate the presence of equatorial Rossby wave activity. Similar SSH responses linked to Rossby waves have been reported in previous studies (e.g., Webber et al., 2014). This basin presents multiple oceanic wave processes such as propagation, reflection, and resonance contributing to the observed SSH pattern as documented by Han (2005).

In the western Pacific, a downwelling KW is already visible in Phase 8, accompanied by strong westerly wind anomalies of up to 3 ms^{-1} in the 150°E–180° region, which are already present in Phase 7. The downwelling KW continues eastward with weaker wind forcing in Phases 8–2, and easterly anomalies in Phases 4–6 contribute to its dissipation near 140ºW. Similarly, an upwelling KW is present in Phase 4 in the western Pacific, also driven by strong easterly wind anomalies that are already present in the two preceding phases. This wave propagates eastward under continued easterly wind anomalies until Phase 7. From Phase 8 onward, winds reverse to westerlies, and the signal weakens near 140ºW. In the eastern Pacific, SSH anomalies are very weak, and no clear pattern can be identified.

In the Atlantic, a weak downwelling KW signal can be observed in the central-western portion of the basin, west of 30ºW longitude, during Phase 3, in association with low-level westerly wind anomalies. This signal appears to be linked to negative OLR anomalies over the Amazon and Africa in the two preceding phases, as shown in Figure 2a. This signal propagates eastward and reaches the eastern Atlantic basin by Phase 7. However, the associated SSH anomalies remain below 1 cm. In addition, SSH negative anomalies suggestive of an upwelling KW are present in the equatorial Atlantic during phase 8 and 1. However, their magnitude is very weak and its propagation not very clear. The previous analysis suggests a connection between MJO occurrence and KW propagation, which is dependent on the basin. There is a clear KW propagation in the Pacific ocean, whereas the signal is very noisy in the Indian ocean and very weak in the Atlantic.

https://doi.org/10.5194/egusphere-2026-4587
Preprint. Discussion started: 3 August 2026

To evaluate the full KW signal in each basin, we now turn our attention to its propagation independently of MJO. To do so, composites of the KW indices are analyzed separately for each basin. Figure 3 shows the SSH and u850 anomalies across different basins for the phases calculated based on the KW index. We remind the reader that the KW indices are independently obtained in each basin, so there is no a priori link between phases in the different basins. In the Indian ocean (Figure 3a), the SSH signal exhibits an equatorial structure in certain regions—for example, in the central part of the basin during Phase 3—which propagates eastward, reaching the Maritime Continent by Phase 6. However, this equatorial signal is accompanied by pronounced off-equatorial SSH anomalies in Phases 2 and 3, suggesting that the oceanic response is not strictly confined to the equator. These off-equatorial contributions reflect the strong baroclinic activity, internal resonances, and boundary reflections that are characteristic of this basin (Han, 2005). Wind anomalies in the Indian ocean associated with KW are more prominent between 60ºE and 90ºE, reaching up to 2.5 m/s at 75°E in phase 4, and -1.5 m/s at the same longitude in phase 8. In contrast, west of 60ºE, wind anomalies rarely exceed 0.5 m/s in magnitude. Positive SSH anomalies are accompanied by easterly wind anomalies in phase 2 and westerly anomalies in phases 3–5. Over the Pacific basin (fig. 3b), westerly winds during phases 7–8 between 120°–150°E initiate a downwelling KW, evident in the SSH field as positive anomalies, which propagates eastward through phase 3 to approximately 160ºW, accompanied by westerly winds. These westerlies reach a peak magnitude of 6 m/s in phase 1 near 180°E. From phase 2 onward, the downwelling KW becomes well-defined near 180ºE, exhibiting a clear KW structure with a strong equatorial signal that decays off the equator. The wave continues propagating eastward without further wind forcing and eventually reaches the American coast during phases 8–1. Next, the Atlantic ocean is shown in Figure 3c. Wind anomalies in this ocean are weak compared to other basins, rarely exceeding 1 m/s in magnitude. However, a westerly wind in phase 1 at 45ºW triggers a downwelling KW that reaches the African coast in phase 5. Finally, the same coherence found between downwelling KWs and wind is also observed between upwelling KWs and wind across the three basins.

These findings highlight the distinct oceanic responses to MJO activity and to phases derived from the KW index across the three tropical ocean basins. While the MJO imprint on SSH anomalies is often diffuse, particularly in the Indian and Atlantic oceans, KW-based phases provide a clearer depiction of equatorial wave dynamics. Notably, westerly and easterly wind anomalies associated with specific MJO phases do at times appear to trigger downwelling and upwelling KWs, respectively, suggesting a potential causal link.

In the following sections, we analyze each ocean basin individually to address our main scientific questions, namely the amount and characteristics of MJOs that trigger KWs, and the later influence of KWs on MJO propagation, with a focus on identifying the relevant processes specific to each region.

https://doi.org/10.5194/egusphere-2026-4587
Preprint. Discussion started: 3 August 2026

4.2 Pacific ocean

MJO/KW	no KW	Phase 1	Phase 2	Phase 3	Phase 4	Phase 5	Phase 6	Phase 7	Phase 8	Σ rows
no MJO	**677 [0.02]**	36 [0.08]	47 [0.29]	36 [0.2]	37 [0.33]	36 [0.28]	*6 [0]*	46 [0.19]	*10 [0]*	931
Phase 1	72 [0.09]	23 [0.1]	**39 [0]**	21 [0.1]	9 [0.72]	1 [0.07]	*0 [0]*	3 [0.08]	20 [0.08]	188
Phase 2	68 [0.17]	8 [0.77]	**28 [0.01]**	**35 [0]**	18 [0.14]	8 [0.62]	*0 [0]*	3 [0.08]	2 [0.18]	170
Phase 3	85 [0.33]	*1 [0.03]*	9 [0.47]	**29 [0.01]**	**41 [0]**	**26 [0.04]**	3 [0.15]	*2 [0.03]*	1 [0.06]	197
Phase 4	89 [0.76]	*0 [0]*	5 [0.18]	3 [0.14]	21 [0.06]	**32 [0]**	**25 [0.01]**	*0 [0]*	4 [0.23]	179
Phase 5	88 [0.25]	*0 [0]*	6 [0.29]	4 [0.19]	1 [0.06]	**27 [0.03]**	**39 [0]**	25 [0.14]	7 [0.51]	197
Phase 6	74 [0.06]	*0 [0]*	3 [0.07]	*0 [0]*	1 [0.05]	4 [0.24]	**41 [0]**	**51 [0]**	22 [0.09]	196
Phase 7	82 [0.43]	19 [0.22]	3 [0.07]	*0 [0]*	*0 [0]*	*0 [0]*	5 [0.51]	**35 [0]**	**30 [0.01]**	174
Phase 8	*68 [0.01]*	**68 [0]**	23 [0.18]	6 [0.38]	*0 [0]*	*0 [0]*	*0 [0]*	7 [0.39]	**33 [0.01]**	205
Σ columns	1303	155	163	134	128	134	119	172	129	2437

Table 1. Contingency table between MJO phases (rows) and Pacific KW index phases (columns). The last row and column represent the marginal totals. "No KW" denotes the days on which the KW PC amplitude is smaller than 1, while "no MJO" refers to the days on which the MJO PC amplitude is smaller than 1. Bold and italic values denote statistically significant occurrences in the upper and lower tails of the distribution, respectively. P-values are shown in brackets.

P(MJO)= 61.8%	P(MJO|KW)= 77.6%	P(MJO|no KW)= 48%
P(KW)= 46.5%	P(no MJO|KW)= 22.4%	P(no MJO|no KW)= 52%
$38.4\% \leq \mathrm{P(KW\|MJO)} \leq 58.4\%$	$51.1\% \leq \mathrm{P(MJO\|KW)} \leq 77.6\%$	

Table 2. Conditional probabilities derived from Table 1.

Table 1 presents the joint distribution of MJO phases and the phases of the Pacific KW Index. A clear phase coherence emerges along the diagonal of the contingency table, where statistically significant positive deviations at the 95% confidence level—indicated in bold—are clustered. Specifically, for a given MJO phase n, an enhanced occurrence of KW phases n, n+1, or n+2 is observed. This diagonal structure suggests a coherent and organized eastward propagation pattern, whereby the progression of MJO convective phases is systematically accompanied by a phase shift in the KW signal. The alignment of significant entries along this diagonal implies a consistent temporal linkage, with MJO convection actively exciting KWs that propagate eastward across the Pacific. Furthermore, the chi-squared analysis reveals a statistically significant dependence between the

https://doi.org/10.5194/egusphere-2026-4587
Preprint. Discussion started: 3 August 2026

MJO and KW indices which supports the presence of a coupling between the two phenomena. According to Table 2, between 38.4% and 58.4% of MJO events generate KWs in the Pacific Ocean ($\mathrm{P(KW|MJO)}$). This range reflects two criteria of association: the lower bound counts only the statistically significant entries of Table 1 (bold entries), whereas the upper bound counts all days with both relevant MJO and KW amplitudes (PC amplitudes greater than 1), in both cases relative to the total number of relevant MJO days (1506 days). Applying the same two criteria, now relative to the number of relevant KW days (1134 days in the Pacific basin), between 51.1% and 77.6% of oceanic KWs in the Pacific are associated with the MJO ($\mathrm{P(MJO|KW)}$). In addition, Table 2 shows that, following a frequentist approach, the probability that a given day has an active phase of the MJO is P(MJO)=61.8%. This probability increases when it is conditioned to active phases of KW (P(MJO|KW)=77.6%), and decreases if conditioned to suppressed phases of KW (P(MJO|no KW)=48%)). These values further indicate that the presence of KW activity substantially increases the likelihood of MJO occurrence relative to its climatological probability, whereas its absence is associated with a marked reduction confirming again that MJO and KW activity are not independent. Conversely, the probability that a given day has an inactive phase of the MJO is P(no MJO)=38.2%. This probability decreases when it is conditioned to active phases of KW (P(no MJO|KW)=22.4%) and increases if conditioned to suppressed phases of KW (P(no MJO|no KW)=52%)). These values demonstrate that the probability of suppressed MJO conditions is substantially reduced in the presence of KW activity relative to its baseline likelihood, whereas it increases markedly when KW activity is absent.

To explore this relationship in greater detail, we contrast the MJO cycle when KW activity is enhanced with that when KW activity is suppressed. To build the former, for each phase of the MJO we select the days that belong to entries in the contingency table where the null hypothesis of independent occurrences of MJO and KW is rejected because it is above the 97.5th percentile, i.e., those entries marked as statistically significant in bold. In turn, the MJO cycle with suppressed KW activity is constructed by composing anomalies of days that pertain to the "no KW" column in table 1. This approach allows us to compare the spatial-temporal characteristics of MJO convection under conditions of enhanced and consistent KW presence versus those where the KW contribution is suppressed or absent. This comparison allows us to characterize how MJO events associated with enhanced, consistent KW activity differ from those in which the KW contribution is suppressed or absent, and to assess the impact of this distinction on SST.

https://doi.org/10.5194/egusphere-2026-4587
Preprint. Discussion started: 3 August 2026

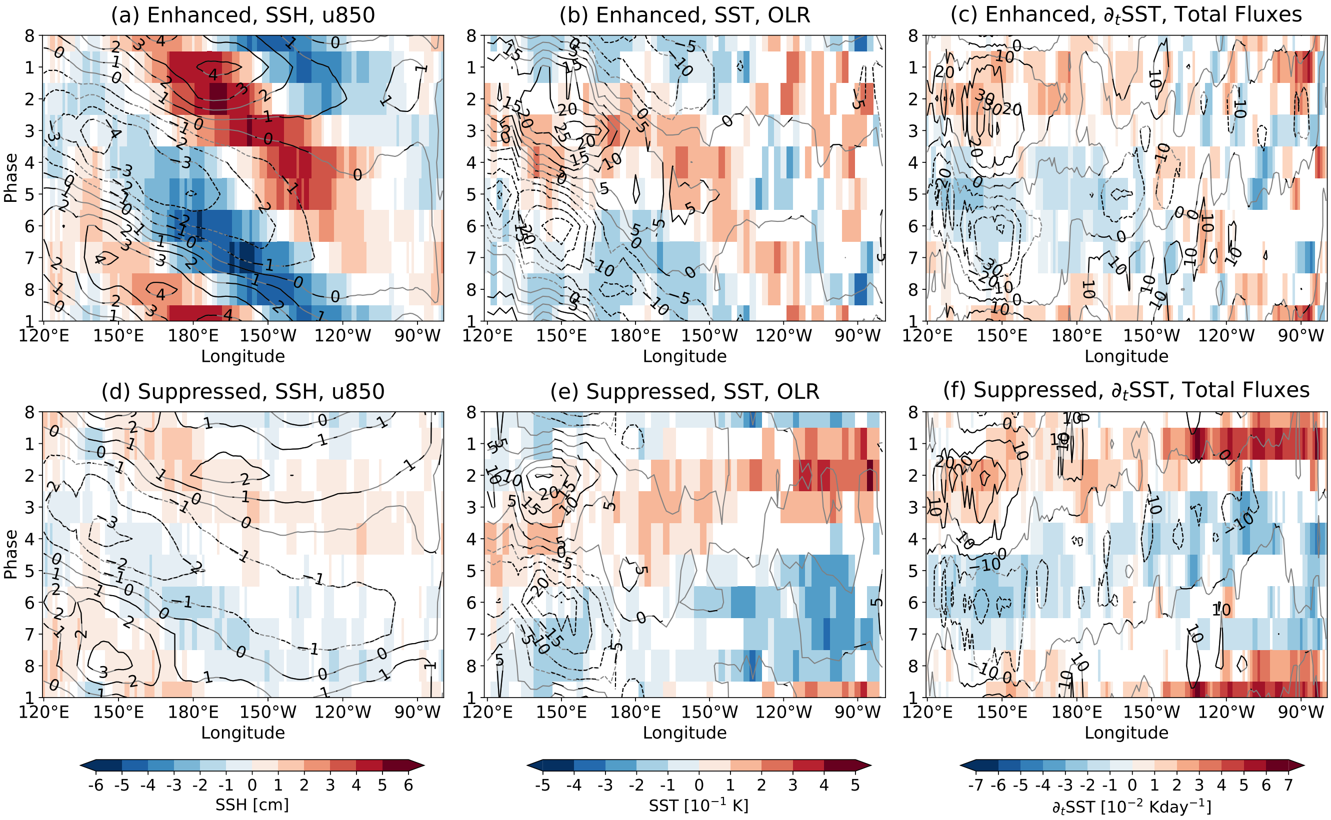

Figure 4. Hovmöller diagrams of MJO phases over the Pacific ocean, averaged between 2°S and 2°N, for anomalies of different variables: (a) SSH (shading in cm) and u850 (contours, from -4 to 4 ms^{-1} in increments of 1 ms^{-1}) during significant phases with enhanced KW activity; (d) same as (a) but for suppressed KW activity in the Pacific. (b) SST (shading in K) and OLR (contours, from -25 to 25 Wm^{-2} in increments of 5 Wm^{-2}) during enhanced KW activity; (e) same as (b) but for suppressed KW activity. (c) ∂_tSST (shading in $Kday^{-1}$) and net surface heat fluxes (contours, from -40 to 40 Wm^{-2} in increments of 10 Wm^{-2}) during enhanced KW activity; (f) same as (c) but for suppressed KW activity. Shaded regions represent only statistically significant anomalies at the 95 $\%$ confidence level, while contour lines are shown in gray for non-significant values and in black for significant values; dashed contours indicate negative values, whereas solid contours denote positive values.

https://doi.org/10.5194/egusphere-2026-4587
Preprint. Discussion started: 3 August 2026

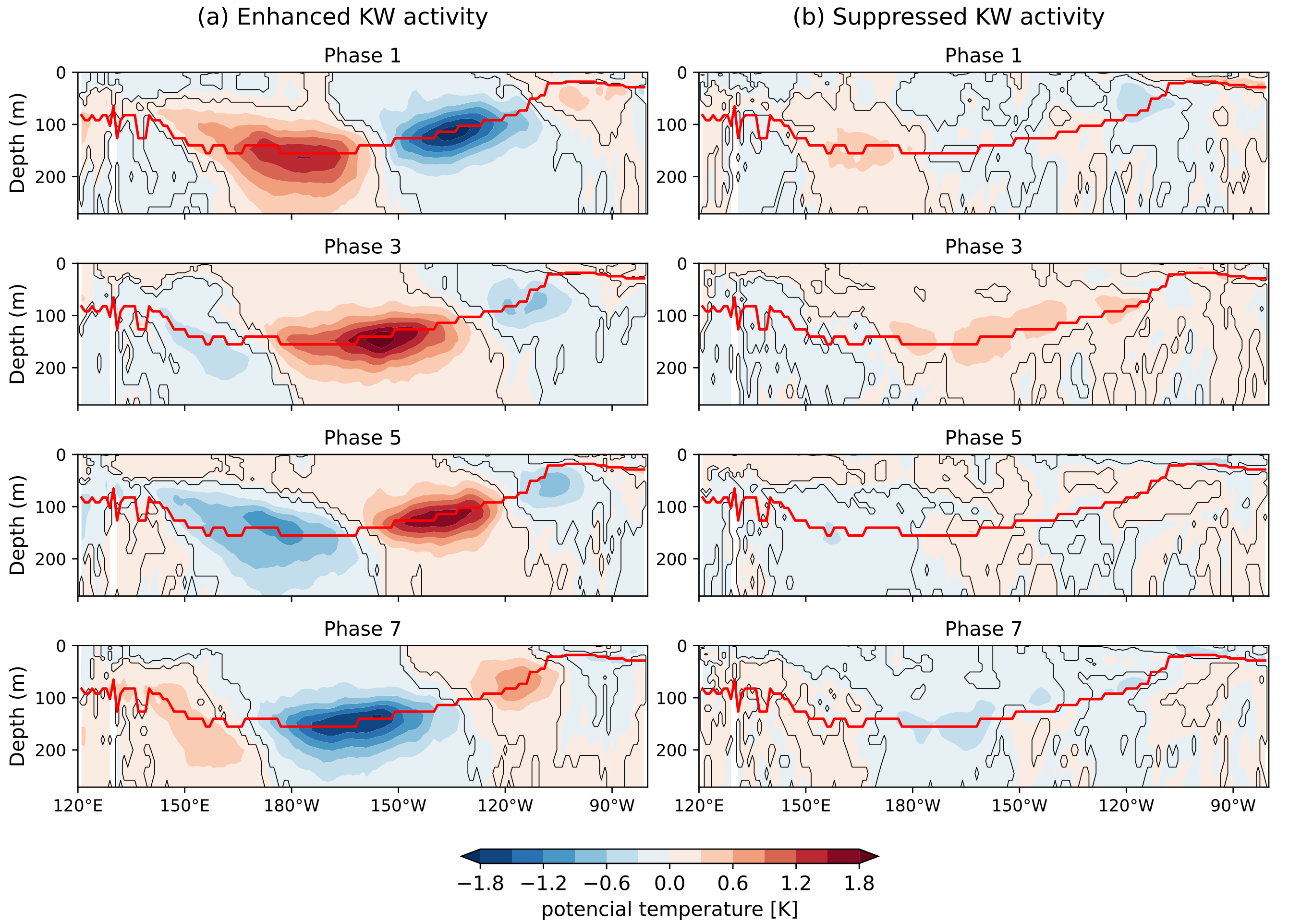

Figure 5. Vertical profiles of potential temperature anomalies (expressed in K) at the equator (latitudinal band between $-0.25°$ and $0.25°$) during the odd phases of the MJO with enhanced KW activity in the Pacific ocean, categorized by the KW index in the Pacific region. Panel (a) corresponds to phases with enhanced KW activity, while panel (b) corresponds to phases with suppressed KW activity. The red line indicates the seasonal thermocline depth (in meters) during DJF. Shading represents the full anomaly field, and contours delineate regions that are statistically significant at the 95% confindence level.

https://doi.org/10.5194/egusphere-2026-4587
Preprint. Discussion started: 3 August 2026

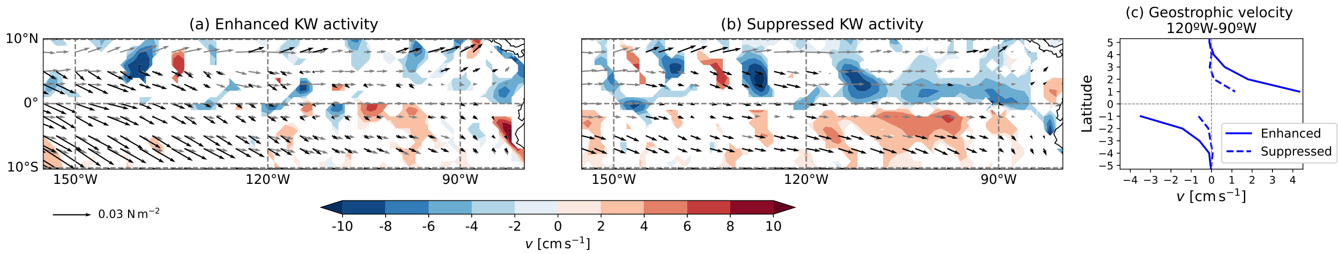

Figure 6. Composites corresponding to MJO phase 1 in the Pacific ocean. (a,b) Meridional surface current (shading, in cms^{-1}) and wind stress (vectors, in Nm^{-2}; reference vector shown in the bottom left corner) for (a) days with enhanced KW activity and (b) days with suppressed KW activity. Shading and vectors show only statistically significant anomalies. Latitudes in (a) and (b) range from 10ºN to 10ºS. (c) Geostrophic velocity (in cms^{-1}) averaged over the 120ºW–90ºW window for the enhanced (solid line) and suppressed (dashed line) cases, computed over a reduced latitudinal range of 5ºN-5ºS.

In figure 4 we compare the MJO cycle when there is enhanced KW activity to that during suppressed KW activity by means of Hovmöller diagrams focused on the equatorial region spanning 2ºN–2ºS. Figure 4a shows that when KW activity is enhanced, the MJO presents u850 anomalies of up to 4 ms^{-1} in magnitude, with a westward extension beyond 140ºW. These are associated with well-defined SSH anomalies, reaching up to 5 cm in magnitude, initiated near 160ºE and propagating continuously and clearly eastward to approximately 80ºW. Figure 4b presents anomalies of OLR and SST in the equatorial Pacific during MJOs with enhanced KW activity. Pronounced OLR anomalies are evident, with magnitudes reaching up to 25 W/m^2, propagating eastward. Regarding SST anomalies, there is a phase lag of approximately two MJO phases, whereby OLR anomalies precede same-signed SST anomalies between 120ºE and 180ºE. East of 160ºW, OLR anomalies weaken considerably, yet SST anomalies continue their eastward propagation toward the American continent. To better understand the contrasted response of SST anomalies described above, we evaluate the anomalies of total heat fluxes, which include radiative and turbulent components, along with ∂_tSST for the enhanced KW activity composites of MJO (Fig. 4c). The total fluxes, which are predominantly radiative (not shown), account for part of the SST variability in the 120ºE–180ºE region where negative flux anomalies cool the ocean and positive anomalies warm it. Beyond 150ºW, SST variations cannot be readily explained by surface heat flux anomalies alone, a point to which we will come back later on. Figure 5 captures the signal of the MJO phases along the equator by displaying vertical potential temperature, which serves as a proxy to infer both vertical and horizontal advection processes, providing further insight into the ∂_tSST illustrated in Figure 4. For MJO propagation associated with enhanced KW activity (Fig. 5a), positive temperature anomalies first appear in phase 7 in the western basin, around 150ºE, at around 120 m depth at the approximate position of the thermocline, coinciding with strong u850 anomalies (Fig. 4a). This anomaly progressively deepens, reaching around 180 m in phase 1 near 180ºE, where it also intensifies, coinciding with strong u850 anomalies (Fig. 4a). Thereafter, and without further coincidence with u850 anomalies, the potential temperature anomaly begins to shoal, reaching approximately 120 m in phase 5 at 130ºW, about 60 m in phase 7 at 110ºW, around 40 m in phase 1 at 90ºW, and ultimately reaching the surface near the American coast in phase 3. Similarly, negative potential temperature anomalies develop in phase 3 near 150º-160ºE, approximately following the thermocline and coinciding with strong westerlies

https://doi.org/10.5194/egusphere-2026-4587
Preprint. Discussion started: 3 August 2026

(Fig. 5a and 4a). These potential temperature anomalies propagate eastward following the thermocline. They are accompaigned by strong westerlies until 180ºE, and eventually reach the surface in phase 7 at 90ºW. In addition, these anomalies exhibit a well-defined structure and are characteristic of KW dynamics, with positive and negative anomalies corresponding to downwelling and upwelling KWs, respectively. Overall, the SST variability appears to be predominantly governed by the propagation of KWs rather than by surface fluxes in the eastern part of the basin.

In contrast, when the KW activity is suppressed (Fig. 4d), wind anomalies are weaker, reaching up to 3 ms^{-1} in magnitude, with a fetch extending to easternmost part of the basin. Consistently, SSH anomalies are weaker, with maximum magnitudes of about 2 cm. These SSH anomalies initiate at approximately 140ºE and propagate to 120ºW, where they stall not clearly propagating to 80ºW. Additionally, for those MJO with suppressed KW activity, OLR anomalies are mainly confined between 100ºE and 180ºE and exhibit lower magnitudes, reaching up to 20 W/m^2 (Fig. 4e). Compared to the case of enhanced KW activity, SST anomalies remain localized and do not show an eastward propagation. Figure 4f presents the anomalies of total surface heat fluxes and ∂_tSST under suppressed KW index conditions. In this case, surface fluxes explain the observed SST changes up to approximately 140ºW. East of this longitude, the flux anomalies are weak, and other mechanisms in phases 1, 2 and 8, such as horizontal advection and latent heat release, appear to be responsible for the observed ∂_tSST, as will be further explored in Figure 6. Lastly, the pattern of ∂_tSST anomalies in the eastern basin is coherent with the SST distribution shown in Figure 4e. In addition, during the MJO propagation when KW activity is suppressed (Fig. 5b), potential temperature anomalies are observed to propagate across the central and western Pacific (150ºE–140ºW), but they are considerably weaker, less coherent, and lack the well-defined vertical structure seen in Figure 5a. East of 140ºW, variations in surface potential temperature appear to be driven primarily by surface forcing rather than by coherent wave dynamics.

To further explore the SST warming observed in the easternmost region (150ºW–90ºW) for MJOs with suppressed KW activity that could not be accounted for by heat fluxes, we present in figure 6 anomalies of meridional surface currents and wind stress vectors for phase 1. Under enhanced KW index conditions, the wind stress remains westerly along the equator, weakening east of 120°W but still retaining its westerly character (Fig. 6a), which contributes to the warming observed in phase 1 of Figure 4c via turbulent fluxes (not shown), particularly east of 100ºW. Conversely, during suppressed KW activity, a marked convergence of meridional surface currents is evident east of 120ºW, characterized by southward flow in the Northern Hemisphere and northward flow in the Southern Hemisphere (Fig. 6b). This pattern leads to the accumulation or convergence of warm surface waters near the equator, therefore warming the eastern part of the basin (Fig. 4f). In this region, winds exert a stronger influence in the suppressed KW than in the enhanced case, particularly during phase 1, when the wind fetch associated with the suppressed KW is more extensive and intense. In both cases, the wind regime generates a Sverdrup transport, driven by the rotational component of the wind stress, that converges toward the equator (not shown) and thereby drives the ∂_tSST signal shown in Figure 4f. In the enhanced KW scenario, however, the geostrophic surface currents associated with the zonal sea level gradient flow in the opposite direction (Figure 6c), so that the resulting anomalous currents are not statistically significant in the 120ºW-90ºW region. These processes collectively enhance equatorial surface water convergence and account for the pronounced warming observed in phase 1 of Figure 4f east of 210°E, which is notably stronger than that in Figure 4c.

https://doi.org/10.5194/egusphere-2026-4587
Preprint. Discussion started: 3 August 2026

In summary, during periods of enhanced KW activity, the MJO in the western basin appears more intense, with stronger low-level winds and more vigorous and longitudinally extended convection, which leads to stronger SST anomalies in the western basin and a clearer propagation both at the surface and at depth compared to the suppressed KW case. In the central and eastern Pacific, the SST patterns differ markedly between enhanced and suppressed KW activity cases. In the enhanced case, SST closely follows the SSH anomalies, reflecting oceanic dynamics with potential temperature anomalies propagating along the thermocline and producing a clear signal at the surface, including in the eastern basin. In contrast, during suppressed KW activity, SST anomalies are largely controlled by surface heat fluxes, except in specific situations such as phase 1 east of 120°W, where wind stress associated with MJO propagation appears to modify meridional currents, suggesting that some oceanic processes are still active which do not seem to be directly related to KW dynamics, but are more consistent with surface-wind–mediated responses.

4.3 Indian ocean

MJO/KW	**no KW**	**Phase 1**	**Phase 2**	**Phase 3**	**Phase 4**	**Phase 5**	**Phase 6**	**Phase 7**	**Phase 8**	**Σ rows**
no MJO	411 [0.39]	62 [0.44]	60 [0.52]	77 [0.88]	66 [0.51]	62 [0.38]	54 [0.65]	72 [0.81]	67 [0.83]	931
Phase 1	91 [0.31]	22 [0.27]	18 [0.54]	7 [0.16]	*0 [0]*	11 [0.49]	8 [0.53]	16 [0.98]	15 [0.5]	188
Phase 2	51 [0.22]	21 [0.3]	**37 [0.01]**	20 [0.51]	3 [0.16]	3 [0.1]	*0 [0]*	11 [0.64]	24 [0.09]	170
Phase 3	53 [0.1]	25 [0.18]	**45 [0.02]**	**48 [0]**	9 [0.68]	*2 [0.02]*	*1 [0.03]*	7 [0.18]	7 [0.33]	197
Phase 4	50 [0.1]	19 [0.35]	12 [0.75]	**37 [0.02]**	**27 [0.04]**	22 [0.32]	4 [0.2]	*2 [0.03]*	6 [0.32]	179
Phase 5	87 [0.64]	3 [0.06]	11 [0.5]	17 [0.83]	13 [0.96]	**32 [0.04]**	26 [0.07]	4 [0.08]	4 [0.1]	197
Phase 6	92 [0.52]	7 [0.35]	*0 [0]*	5 [0.06]	8 [0.6]	27 [0.23]	**27 [0.04]**	27 [0.07]	3 [0.08]	196
Phase 7	71 [0.1]	*3 [0.05]*	*2 [0.03]*	*4 [0.04]*	9 [0.67]	26 [0.08]	23 [0.11]	25 [0.06]	11 [0.9]	174
Phase 8	78 [0.73]	22 [0.49]	8 [0.38]	*0 [0]*	16 [0.58]	15 [0.86]	13 [0.93]	29 [0.16]	24 [0.24]	205
Σ columns	984	184	193	215	151	200	156	193	161	2437

Table 3. As in Table 1, but limited to the Indian ocean region.

P(MJO)= 61.8%	P(MJO|KW)= 64.2%	P(MJO|no KW)= 58.2%
P(KW)= 59.6%	P(no MJO|KW)= 35.8%	P(no MJO|no KW)= 41.8%
$16.8\% \leq \mathrm{P(KW\|MJO)} \leq 62\%$	$17.4\% \leq \mathrm{P(MJO\|KW)} \leq 64.2\%$	

Table 4. Conditional probabilities derived from Table 3.

https://doi.org/10.5194/egusphere-2026-4587
Preprint. Discussion started: 3 August 2026

Table 3 displays the joint distribution of MJO and Indian KW phases. As with the Pacific, a diagonal phase relationship is present, with significant positive deviations marked in bold; however, it is less pronounced than in the Pacific. Notably, MJO phases 1, 7, and 8 lack any significant associations, and the enhancement is mostly limited to phase pairs like (n–1, n) and (n, n), where n refers to the MJO phase and the second element to the Indian KW phase. A chi-squared test confirms a significant statistical dependence between the MJO and KW indices over the Indian ocean.

According to Table 4, between 16.8% and 62% of MJO events generate KWs in the Indian ocean. Conversely, between 17.4% and 64.2% of oceanic KWs in the Indian ocean are associated with the MJO. These percentages are computed following the procedure describe in Section 4.2. Moreover, the values in Table 4 indicate that KW activity has a modest influence on MJO occurrence, slightly increasing its probability when present (from 61.8% to 64.2%), slightly decreasing it when KWs are absent (from 61.8% to 58.2%). Correspondingly, the probability of no MJO conditioned on the absence of KWs, P(MJO|no KW) = 35.8%, is slightly lower than the unconditional probability of no MJO, P(no MJO) = 38.2%. Overall, the dependence between MJO and KW activity in this region is weaker than that reported in Table 2 for the Pacific.

To investigate this relationship in the Indian ocean, we begin by performing a composite analysis similar to the one used for the Pacific case. To characterize enhanced KW activity in the Indian ocean for each MJO phase, we select the days that belong to entries in table 3 highlighted as bold. For MJO phases lacking such significant bold entries—specifically phases 1, 7, and 8—we select values with the lowest p-values just above the significance threshold, including entries KW phases 1, 7 and 7 for MJO phases 1, 7 and 8, respectively. In turn, to construct MJO phases with suppressed KW activity in the Indian ocean, we compose anomalies of days that pertain to the ”no KW” column in table 3.

https://doi.org/10.5194/egusphere-2026-4587
Preprint. Discussion started: 3 August 2026

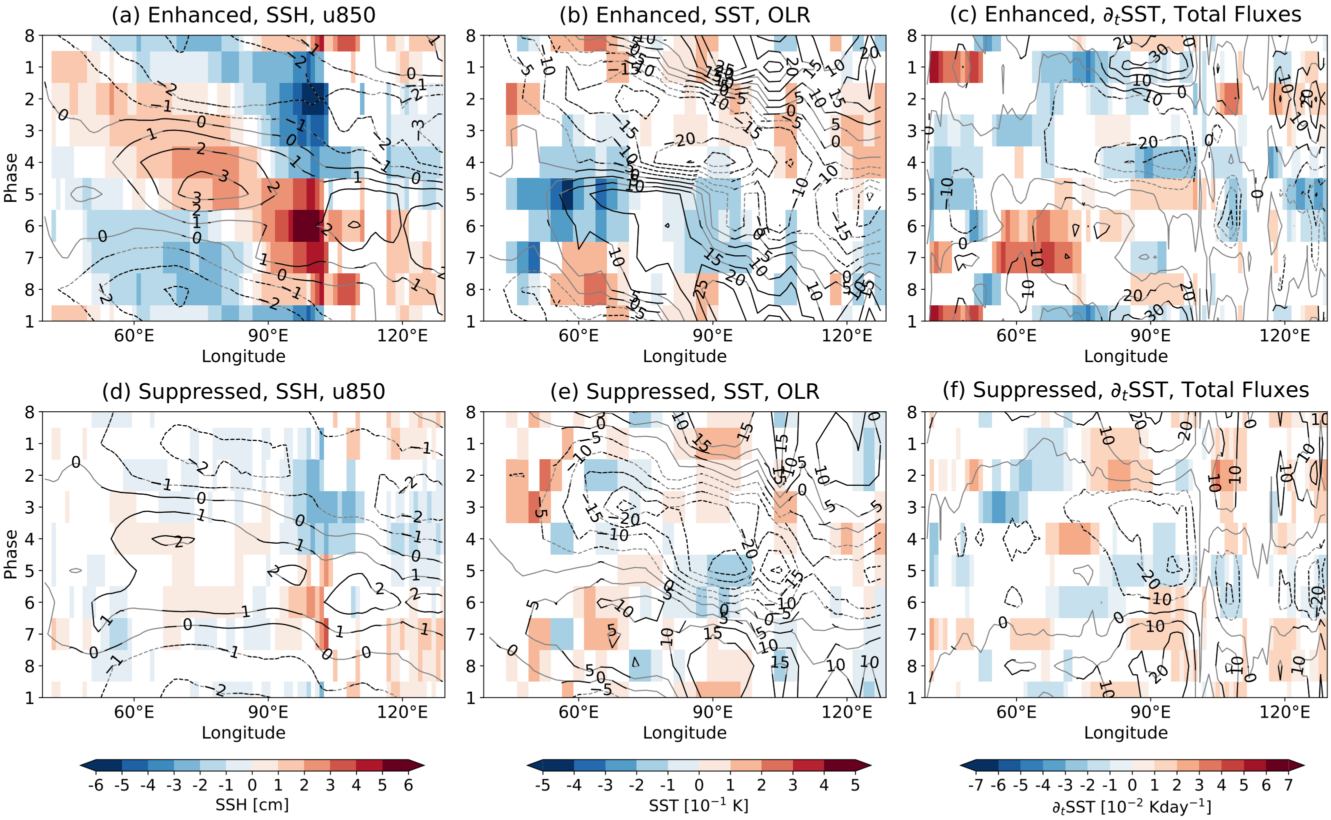

Figure 7. As in Figure 4 but for the Indian ocean.

Figure 7a displays anomalies of SSH and u850 associated with the MJO cycle for conditions of enhanced KW activity in the Indian ocean. SSH anomalies exhibit the strongest signals between 75ºE and 100ºE, with a marked maximum near 100ºE, while anomalies are weak west of 50ºE, indicating suppressed variability in the western Indian ocean. The low-level zonal wind anomalies reach peak magnitudes near 75ºE, surpassing 3 ms^{-1}, suggesting strong lower-tropospheric wind activity concentrated in the central part of the basin. These patterns reflect enhanced dynamical coupling during strong KW activity, with the observed SSH and low-level zonal wind anomalies consistent with increased generation and eastward propagation of equatorial KWs. MJO-related OLR anomalies when KW activity is enhanced exhibit a clear eastward propagation across the equatorial Indian ocean, maintaining a coherent structure and amplitude throughout the basin (Fig. 7b). In contrast, the SST anomalies display a more erratic eastward displacement, with their propagation stalling during phases 5–7. We, therefore, turn our attention to MJO-related surface heat fluxes and to the temporal derivative of SSTs, which, during enhanced KW activity, show a general coherent spatial and temporal alignment across most of the basin (Fig. 7c). Positive heat flux anomalies into the ocean are typically associated with warming SSTs, and negative heat flux anomalies with SST cooling, reflecting effective air-sea coupling, except during MJO phase 1 near 90ºE, where the flux anomaly does not correspond with the time derivative of SSTs, suggesting influences from ocean subsurface processes.

https://doi.org/10.5194/egusphere-2026-4587
Preprint. Discussion started: 3 August 2026

Conversely, when the activity of KW is suppressed, MJO-related SSH anomalies are substantially weaker and more spatially limited, with reduced amplitudes across the basin (Fig. 7d). In addition, low-level zonal wind anomalies are smaller, with maximum u850 anomalies reaching 2 ms^{-1} near 75ºE and, as for the enhanced KW activity case, they remain negligible west of 50ºE. OLR anomalies remain coherent in the suppesed KW activity scenario (Fig. 7e) and exhibit an eastward propagation similar to that observed in Figure 7b, although maximum OLR anomalies are reduced, especially for the suppressed convection MJO phases 8 and 1 and in the eastern part of the basin, consistent with weaker low-level winds. SST anomalies lack a clear dynamical pattern and do not present a discernible propagative structure, though their anomalies tend to lag by approximately one phase OLR maximum and minimum peaks between 80ºE and 100ºE, suggesting that MJO-related radiative and surface heat effects could be governing the SST response there. In this case, SST anomalies are less pronounced throughout the basin than in the enhanced KW scenario. For the suppressed KW activity, the alignment between surface heat flux anomalies and the time derivative of SST is generally maintained, though with reduced amplitude and spatial coherence (Fig. 7f).

https://doi.org/10.5194/egusphere-2026-4587
Preprint. Discussion started: 3 August 2026

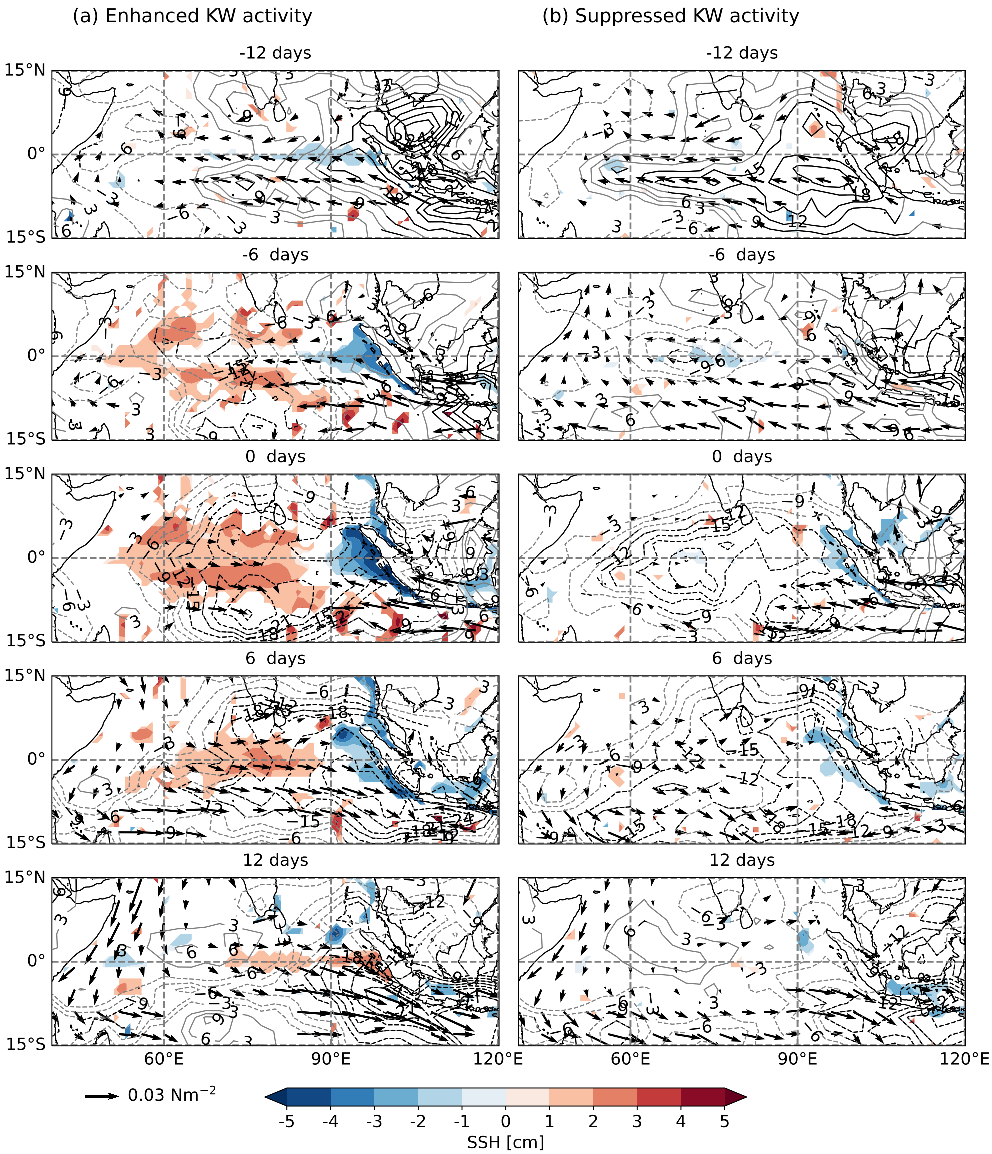

Figure 8. Lead–lag composites for different MJO events in the Indian ocean: SSH (shading in cm), OLR (contours; from -24 to 24 Wm^{-2} in increments of 3 Wm^{-2}), and wind stress (vectors in Nm^{-2}; reference vector shown in the bottom left corner). (a) Events centered on the central days identified when both MJO and KW activity are in Phase 3 from Table 1; (b) events centered on the central days identified when MJO is in phase 3 while KW activity is suppressed. Shading and vectors display only statistically significant anomalies at the 95% confidence level; gray contours indicate non-significant values, black contours indicate significant values, dashed contours represent negative values, and solid contours denote positive values.

https://doi.org/10.5194/egusphere-2026-4587
Preprint. Discussion started: 3 August 2026

Unlike in the Pacific case, the previous analysis in the Indian ocean included three MJO phases for which there was no statistically significant entry with enhanced KW activity in table 3 (phases 7, 8, and 1), which hinders the analysis of the MJO evolution. To complement it, we select particular MJO events and track their evolution for cases with enhanced and suppressed KW activity. Among the various possibilities, we select events based on phase 3 of the MJO, which is a phase of enhanced convection in the central part of the basin (around 75ºE) and which exhibits the highest number of days coinciding with a particular phase of KW (phase 3: 48 days) and also one of the smallest numbers of non-KW occurrences (53, with the smallest p-value). Among all days that pertain to each of those two entries, we select only independent events, choosing the central day of the event as the starting point, and build a composite using all the events. A total of 13 MJO events were identified for the enhanced KW case and 16 for the suppressed KW case. To examine the temporal evolution, we perform lead-lag analysis from –12 to +12 days of these central days. Figure 8 displays anomalies in SSH, OLR, and surface wind stress for the MJO events with enhanced KW activity in the Indian ocean (left panel) and with suppressed KW activity (right panel). In Figure 8a, by day –12, positive OLR anomalies indicative of stable atmospheric conditions are observed over the central and eastern Indian ocean. Beginning around day –6, negative OLR anomalies emerge in the western basin and propagate eastward, also reaching the Maritime Continent by day +12. These negative anomalies are more pronounced than the preceding positive values, reflecting a more substantial convective response. In parallel, a positive SSH anomaly west of 60°E around day –6 develops, which progresses eastward and reaches regions east of 90°E by day +12. Subsequently, on days 0, 6, and 12, westerly anomalies between 60°E and 100°E accompany the positive SSH anomaly, indicating wind forcing supportive of downwelling conditions. The spatial structure of the SSH field evolves from a broad, off-equatorial pattern, especially evident on days –6 and 0, to a more equatorially confined configuration by days +6 and +12. This transition appears to reflect a dynamical adjustment toward a coherent, equatorially trapped KW structure. It may correspond to a Rossby-to-Kelvin transition: the signal at lag -6 suggests the presence of a preceding Rossby wave, after which the wind anomalies begin to favor the development of a KW, with well-defined westerlies evident by lag 0.

Conversely, for the MJO events in which KW activity is suppressed, the OLR field exhibits a dipolar temporal pattern: positive anomalies from day –12 east of 50°E, followed by negative anomalies from day –6 to +12 (Fig. 8b). In contrast, the SSH field remains disorganized, with weak, spatially noisy anomalies and no coherent eastward propagation. No clear signals indicative of equatorial KW activity are identifiable throughout the period. Regarding the surface wind stress field, although some features could potentially support wave generation as easterly anomalies found on days –12 and –6, no consistent SSH response is detected. On days 6 and 12, wind anomalies are predominantly off-equatorial. Finally, zonal wind stress is stronger along the equator under enhanced than suppressed conditions. This suggests that both the intensity of equatorial surface winds and the appropriate timing of wind anomaly onset, occurring after the onset of oceanic Rossby waves (Fig. 8a, lags -6 and 0), play a key role in the excitation and maintenance of KWs. This is clearly illustrated by comparing lags 0, 6, and 12 in Figures 8a and 8b.

https://doi.org/10.5194/egusphere-2026-4587
Preprint. Discussion started: 3 August 2026

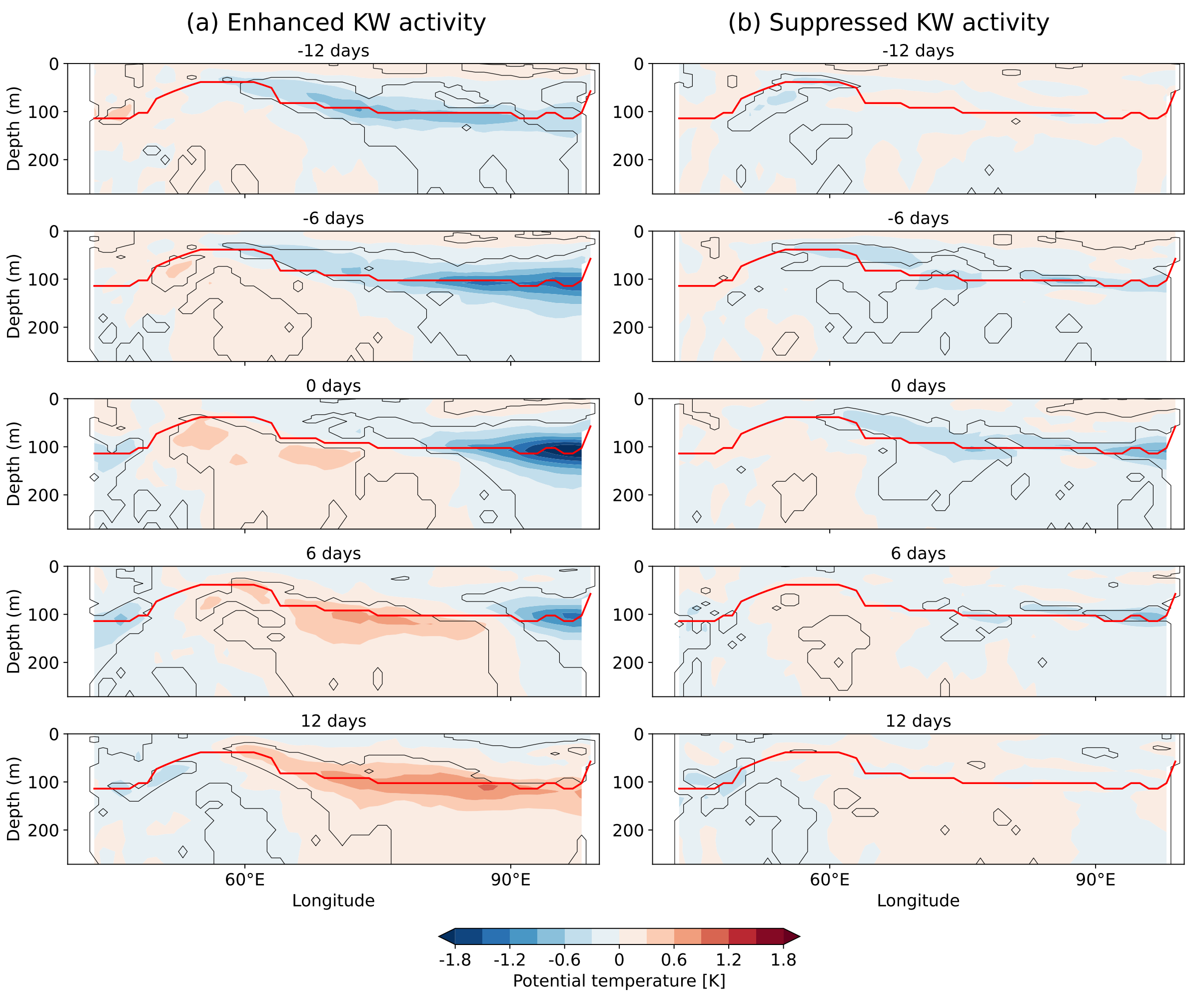

Figure 9. Vertical profiles of potential temperature anomalies (expressed in K) at the equator (within a latitudinal band of $\pm 0.25°$) during different lead–lag days of MJO events in the Indian ocean region. Panel (a) corresponds to MJO events during periods of enhanced KW activity, while panel (b) corresponds to MJO events during suppressed KW activity. These correspond to the composites shown in Figure 8. The red line indicates the seasonal thermocline depth (in meters) during DJF. The full anomaly is shaded, with contours marking the separation between significant and non-significant areas at the 95% confidence level.

Figure 9 shows depth–longitude sections of potential temperature anomalies, averaged across the latitudinal band of -0.25°, 0°, and 0.25°, to analyze equatorial footprint in the subsurface thermal structure for the selected MJO events. In the case of MJO events with enhanced KW activity in the Indian ocean, a pronounced negative temperature anomaly appears near 80ºE around day -12 and propagates eastward, reaching approximately 100ºE between days -6 and 0. In parallel, a positive temperature anomaly develops east of 60ºE around day -6 and progresses eastward, reaching 70ºE by day 0, 75ºE by day 6,

https://doi.org/10.5194/egusphere-2026-4587
Preprint. Discussion started: 3 August 2026

and extending beyond 80ºE by day 12. Throughout the evolution, both negative and positive anomalies exhibit their maximum amplitude near 100 meters depth, coinciding with the thermocline. The spatial and temporal characteristics of these anomalies, namely their coherent eastward propagation, vertical confinement around the thermocline, and alternating sign, are consistent with the canonical structure of equatorial KWs. The negative anomaly corresponds to an upwelling KW, while the positive anomaly reflects a downwelling counterpart. These subsurface signals are also in agreement with SSH anomalies shown in Figure 8a, further supporting their interpretation as KWs. However, the surface temperature shows a trend opposite to that of the subsurface, reflecting the possible impact of radiative heat fluxes.

For the suppressed KW activity case, the composite of the selected MJO events displays subsurface temperature anomalies associated with a less clearly defined signal (Fig. 9b). A negative temperature anomaly appears east of 60ºE at day -12 and propagates eastward, reaching 100ºE by day 6. Although the anomaly is centered near 100 meters depth, its structure is less coherent than in Figure 9a. A weak positive anomaly also appears near 60ºE on day 6, but it gradually diminishes and becomes negligible by day 12. Despite the lower signal-to-noise ratio, the observed eastward propagation and vertical confinement suggest the presence of a weaker and less organized KW. Although a signal is present in the corresponding SSH field in Figure 8b, it is relatively weak and appears to lack either the amplitude or the timing necessary to effectively excite and subsequently support the development of the KWs in the suppressed KW case, yet the temperature anomalies in Figure 9b still reveal KW-like characteristics.

In summary, during enhanced KW activity, the MJO in the Indian ocean exhibits strong dynamical coupling, with pronounced SSH anomalies between 75°E and 100°E and low-level zonal winds exceeding 3 m/s near 75°E. However, the impact of KW activity on the MJO appears less clear than in the Pacific, where SST variability is more directly controlled by KW dynamics. In the Indian ocean, surface fluxes seem to explain most of the SST changes. OLR anomalies propagate coherently eastward, while SST anomalies display an erratic displacement and tend to stall during all phases. Surface heat flux anomalies generally align with SST tendencies, except for localized mismatches at 90°E in phase 1, suggesting subsurface influence. Lead–lag analysis based on events centered in phase 3 of the MJO reveals that, concurrent with strong convection over the central Indian ocean, SSH anomalies transition from negative to positive phases, accompanied by easterly and westerly wind stress anomalies that support upwelling and downwelling conditions, respectively. In particular, downwelling anomalies during enhanced KW activity are associated with strong equatorial westerly wind anomalies in the central basin (60°E–90°E) at lags 0, +6, and +12 days. Subsurface temperature anomalies propagate eastward along the thermocline with alternating signs, consistent with the canonical KW structure. In contrast, during suppressed KW activity, SSH and wind anomalies are weaker and lack coherent propagation. Although OLR anomalies continue to propagate eastward, their amplitude is reduced, and SST anomalies do not exhibit a clear dynamical structure, appearing largely governed by surface heat fluxes. Subsurface signals are present but less organized than in the enhanced KW case. The key factors limiting the MJO impact under suppressed KW conditions appear to be the timing of wind anomalies, which leads to a phase relationship unfavorable for KW generation, and the weaker equatorial wind anomalies compared to the enhanced case. Specifically, negative zonal wind anomalies in the central basin (70°E) at lags -12, -6 days coincide with a positive Rossby wave signal, likely associated with a prior reflection event.

https://doi.org/10.5194/egusphere-2026-4587
Preprint. Discussion started: 3 August 2026

4.4 Atlantic ocean

MJO/KW	no KW	Phase 1	Phase 2	Phase 3	Phase 4	Phase 5	Phase 6	Phase 7	Phase 8	Σ rows
no MJO	453 [0.58]	81 [0.5]	41 [0.18]	34 [0.6]	60 [0.6]	55 [0.94]	80 [0.59]	43 [0.43]	84 [0.94]	931
Phase 1	86 [0.8]	10 [0.54]	13 [0.91]	*0 [0]*	*4 [0.04]*	17 [0.44]	18 [0.61]	21 [0.11]	19 [0.55]	188
Phase 2	76 [0.81]	28 [0.08]	16 [0.53]	4 [0.26]	*5 [0.06]*	14 [0.7]	22 [0.19]	3 [0.29]	*2 [0.04]*	170
Phase 3	55 [0.06]	19 [0.59]	**41 [0]**	12 [0.79]	14 [0.53]	8 [0.38]	12 [0.79]	14 [0.51]	22 [0.49]	197
Phase 4	77 [0.94]	10 [0.82]	22 [0.15]	16 [0.28]	15 [0.95]	*2 [0.04]*	9 [0.51]	6 [0.48]	22 [0.31]	179
Phase 5	87 [0.93]	6 [0.27]	6 [0.2]	19 [0.13]	27 [0.27]	20 [0.33]	6 [0.15]	5 [0.36]	21 [0.56]	197
Phase 6	83 [0.75]	9 [0.51]	16 [0.58]	17 [0.22]	**32 [0.05]**	12 [0.82]	21 [0.57]	1 [0.06]	5 [0.07]	196
Phase 7	67 [0.38]	7 [0.38]	6 [0.39]	14 [0.29]	**34 [0.01]**	17 [0.39]	6 [0.14]	9 [0.95]	14 [0.92]	174
Phase 8	103 [0.56]	6 [0.25]	3 [0.08]	1 [0.06]	13 [0.74]	11 [0.84]	14 [0.96]	**34 [0.03]**	20 [0.71]	205
Σ columns	1087	176	164	117	204	156	188	136	209	2437

Table 5. As in Table 1, but limited to the Atlantic ocean region.

P(MJO)= 61.8%	P(MJO|KW)= 64.6%	P(MJO|no KW)= 58.3%
P(KW)= 55.4%	P(no MJO|KW)= 35.4%	P(no MJO|no KW)= 41.7%
$9.4\% \leq \mathrm{P(KW|MJO)} \leq 57.9\%$	$10.4\% \leq \mathrm{P(MJO|KW)} \leq 64.6\%$	

Table 6. Conditional probabilities derived from Table 5.

Table 5 illustrates the joint distribution of MJO and Atlantic KW phases. In contrast to the results obtained for the Pacific and, to a lesser extent, Indian basins, no diagonal pattern of statistically significant positive deviations, marked in bold, is evident. Only phases 3, 6, 7, and 8 of the MJO cycle present statistically significant positive signals for KW phases in the Atlantic 2, 4, 4 and 7, respectively. However, the chi-squared test of independence reveals a statistically significant dependence between the KW and MJO activity in this basin.

According to Table 6, between 9.4% and 57.9% of MJO events generate KWs in the Atlantic ocean. Conversely, between 10.4% and 64.6% of oceanic KWs in the Atlantic ocean are associated with the MJO. These percentages are computed following the procedure describe in Section 4.2. The conditional probabilities shown in table 6 indicate that KW activity has a modest influence on MJO occurrence, slightly increasing its probability when present (from 61.8% to 64.6%). Correspondingly, the probability of no MJO conditioned on the absence of KWs, P(MJO|no KW) = 35.4%, is slightly lower than the unconditional

https://doi.org/10.5194/egusphere-2026-4587
Preprint. Discussion started: 3 August 2026

probability of no MJO, P(no MJO) = 38.2%. Overall, the dependence between MJO and KW activity in this region is weaker than that reported in Table 2 for the Pacific and similar to table 3 for the Indian ocean.

To explore this relationship in greater detail, we apply a lead–lag compositing analysis based on event selection. Given the limited number of significantly positive associations, we selected the events based on phase 3 of the MJO. Over the Atlantic basin, phase 3 of the MJO shows enhanced convection over the easternmost part of the basin, already weakening (Fig. 2a) and presents the highest number of days coincident with a particular phase of KW in the Atlantic (phase 2). Among the possible 41 days, we take the central day of each independent MJO event as day 0 to characterize the MJO events with enhanced KW activity, resulting in a total of 9 events. In turn, to characterize MJO events with suppressed KW activity, we apply the same methodology to the events inside the pool of 55 days that were catalogued as pertaining to phase 3 of the MJO and to a suppressed KW activity leading to 16 selected events.

https://doi.org/10.5194/egusphere-2026-4587
Preprint. Discussion started: 3 August 2026

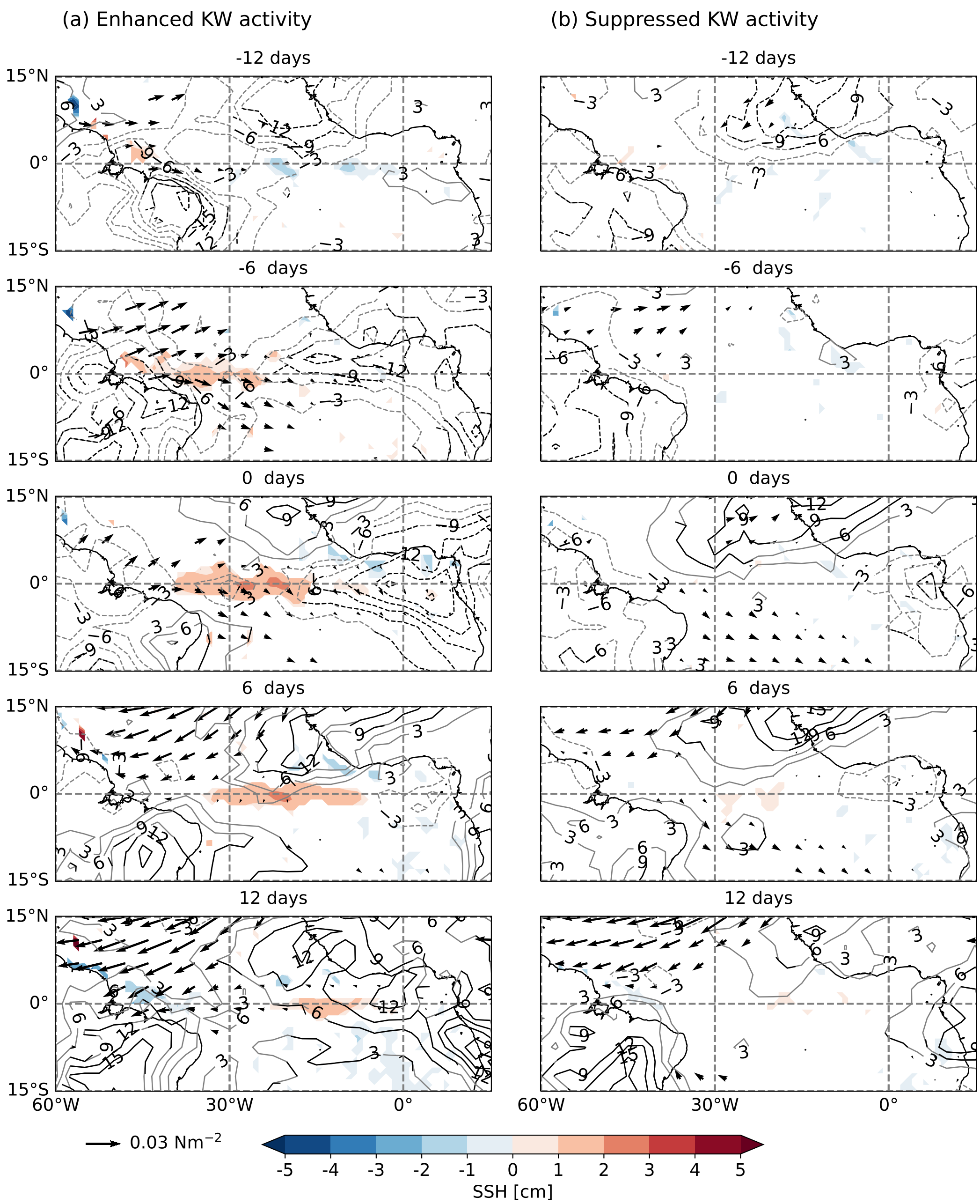

Figure 10. Lead–lag composites for different MJO events in the Atlantic ocean: SSH (shading in cm), OLR (contours; from -24 to 24 Wm^{-2} in increments of 3 Wm^{-2}), and wind stress (vectors in Nm^{-2}; reference vector shown in the bottom left corner). (a) Events centered on the central days identified when MJO is in Phase 3 while KW activity is in Phase 2 from Table 5; (b) events centered on the central days identified when MJO is in phase 3 while KW activity is suppressed. Shading and vectors display only statistically significant anomalies at the 95% confidence level; gray contours indicate non-significant values, black contours indicate significant values, dashed contours represent negative values, and solid contours denote positive values.

https://doi.org/10.5194/egusphere-2026-4587
Preprint. Discussion started: 3 August 2026

We begin the analysis of MJO events by examining their main characteristics and their imprint over the Atlantic. As an initial step, we focus on the ocean–atmosphere interaction as illustrated in Figure 10, which presents anomalies in OLR, SSH, and wind stress. Figure 10a presents a lead-lag composite of anomalies for MJO events when KW activity is enhanced in the Atlantic basin. On day -12, significant negative OLR anomalies are observed over Brazil, indicating enhanced convection. This convective activity is associated with strong westerly surface winds that initiate a downwelling KW, forming near the South American coast around the equator. These westerly wind anomalies intensify the development and propagation of the KW on days -6 and 0, allowing the wave to travel toward the central basin. From day 6 onward, the wave continues its eastward propagation in the absence of significant wind anomalies, while easterly winds develop along the Brazilian coast, accompanied by positive OLR anomalies, indicative of suppressed convection and negative SSH anomalies emerging from day +12. For the suppressed KW activity case, figure 10b shows the lead-lag composite of OLR, SSH, and wind stress anomalies. Prior to day 6, weak wind anomalies are present along the Brazilian coast, while no wind anomalies are observed at the equator, indicating forcing insufficient to generate a significant SSH response. From day 6 onward, stronger easterly winds develop in the off-equatorial region west of 10°W, whereas equatorial winds remain negligible and do not coincide with a clear SSH signal. OLR anomalies over Brazil remain weak throughout, except for a marked enhancement on day 12. In contrast, significant OLR anomalies are detected over the Guinea Dome region, with negative values at day -12 and positive anomalies at days 0 and 6, indicating a distinct convective evolution unrelated to the SSH response observed in the enhanced KW activity case. Finally, at all lags, OLR anomalies along the equatorial African coast are very weak, consistent with the absence of equatorial westerly winds.

https://doi.org/10.5194/egusphere-2026-4587
Preprint. Discussion started: 3 August 2026

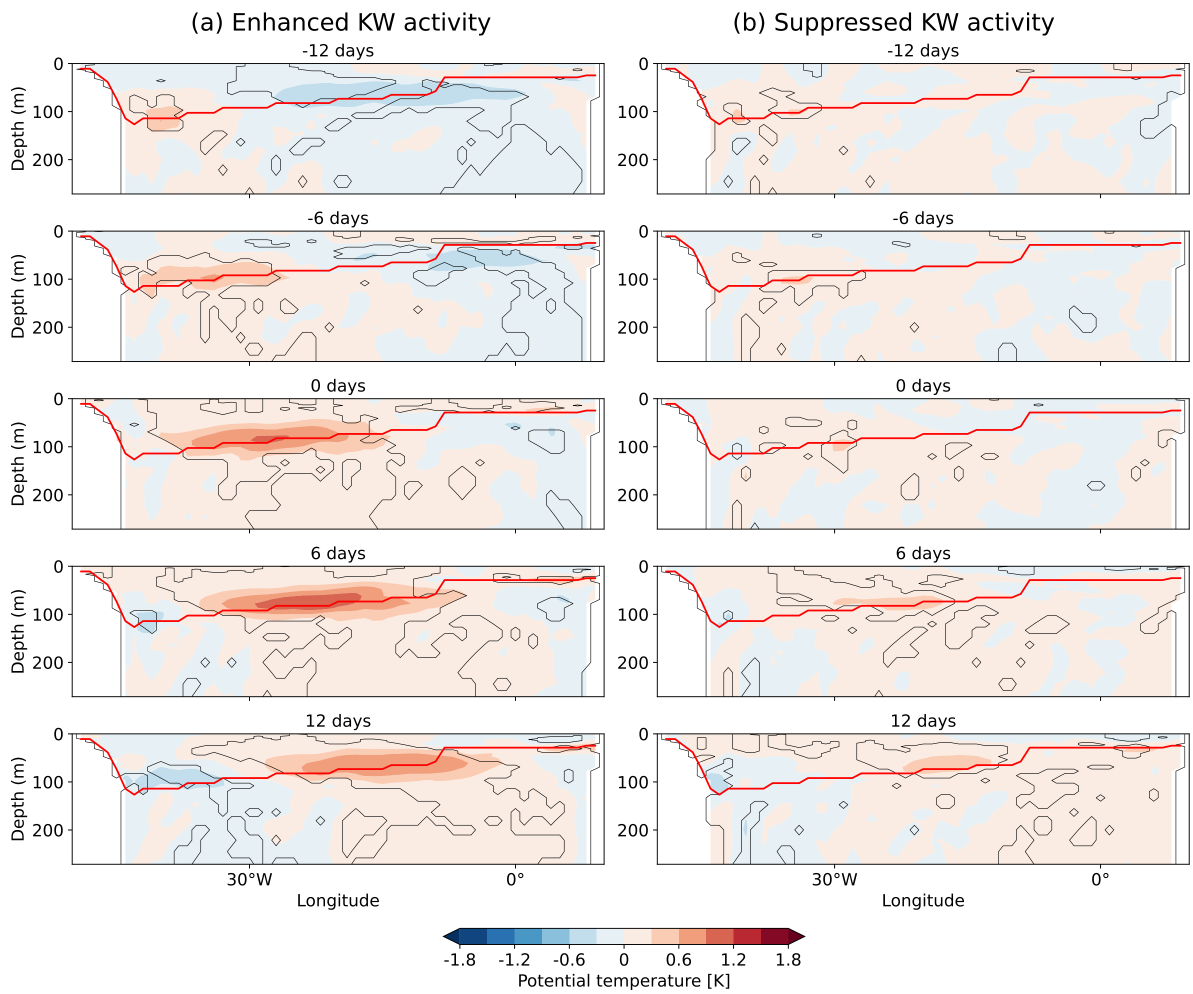

Figure 11. Vertical profiles of potential temperature anomalies (expressed in K) at the equator (within a latitudinal band of $\pm 0.25°$) during different lead–lag days of MJO events in the Atlantic ocean region. Panel (a) corresponds to MJO events during periods of enhanced KW activity, while panel (b) corresponds to MJO events during suppressed KW activity. These correspond to the composites shown in Figure 10. The red line indicates the seasonal thermocline depth (in meters) during DJF. The full anomaly is shaded, with contours marking the separation between significant and non-significant areas at the 95% confidence level.

As shown in Figures 5 and 9, the vertical temperature structure provides a robust variable for identifying and tracking the evolution and propagation of KWs through the thermocline. Figure 11 presents the potential temperature anomalies for cases of enhanced and suppressed KW activity in the Atlantic. In the enhanced KW activity case analyzed along the equator, the SSH anomalies identified as downwelling in Figure 10a exhibit a clear subsurface signature within the thermocline. In the suppressed case, anomalies consistent with a KW signal are also present, although they are notably weaker.

https://doi.org/10.5194/egusphere-2026-4587
Preprint. Discussion started: 3 August 2026

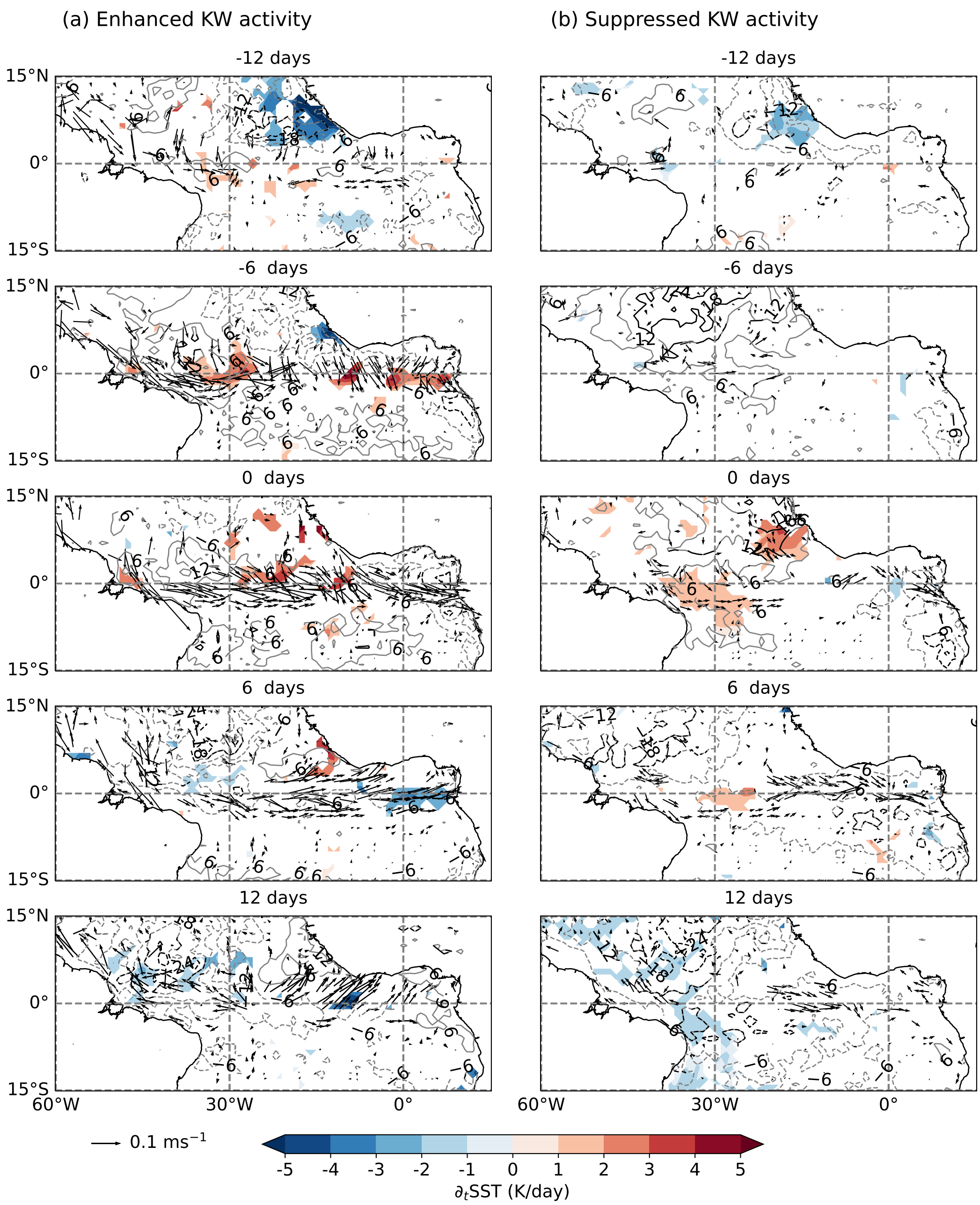

Figure 12. Lead–lag composites for the same MJO events as in Figure 10 in the Atlantic ocean: ∂_tSST (shading in $Kday^{-1}$), total fluxes anomalies (contours; from -18 to 18 Wm^{-2} in increments of 6 Wm^{-2}, omitting the 0 Wm^{-1} level), and surface current anomalies (vectors in ms^{-1}; reference vector shown in the bottom left corner). (a) MJO events with enhanced KW activity; (b) MJO events with suppressed KW activity. Shading and vectors display only statistically significant anomalies at the 95% confidence level; gray contours indicate non-significant values, black contours indicate significant values, dashed contours represent negative values, and solid contours denote positive values.

https://doi.org/10.5194/egusphere-2026-4587
Preprint. Discussion started: 3 August 2026

To provide a more comprehensive view of the local ocean–atmosphere interaction induced by MJO events at the ocean surface, we present in Figure 12a the lead-lag composite of ∂_tSST anomalies, total surface heat fluxes, and current velocities for the enhanced KW activity case. In the central and western equatorial Atlantic, the ∂_tSST anomalies are associated with oceanic processes. Around day -6 we observe a heating in the west Atlantic associated with the downwelling KW described in Figure 10. This dynamical signal results in SST warming in the central equatorial Atlantic around day 0 as the wave continues its eastward propagation. In addition, there is a cooling in the western basin from approximately day +6 onward consistent with the sign of the surface fluxes anomalies. In the eastern part of the basin, ∂_tSST anomalies appear to be primarily driven by surface ocean currents. As shown in Figure 12a, the warming around days -6 and 0 coincides with anomalous northwesterly currents toward the equator, which causes anomalous horizontal advection that warms the eastern equator. Conversely, the cooling on days +6 and +12 is associated with anomalous westerly and southwesterly currents respectively; therefore, the horizontal advection caused by the mean currents, due to the anomalous zonal gradient in SST driven by the KW, could explain the cooling in the eastern equator. Surface heat flux anomalies in this region are again weak and play a limited role in shaping the SST response. Conversely, over the Guinean Dome, changes in SSTs seem to respond to modifications in heat fluxes: the strong cooling tendency shown on day -12 are consistent with the negative surface flux anomalies there. These heat anomalies arise from the radiative component and are accompained by OLR anomalies as shown in Fig. 10a. The negative tendency in SSTs in the Guinean Dome weakens on day -6, following a weakening in the surface flux anomalies. Figure 12b corresponds to the case of suppressed KW activity. The most evident feature is that, across the equatorial region and throughout the basin, ∂_tSST anomalies are weaker and do not exhibit a consistent relationship with ocean current anomalies. In some instances, the ∂_tSST anomalies are consistent with the surface fluxes anomalies (e.g., days 0 and +12), whereas in others they are not (e.g., day +6). In the Guinea Dome region, the signal also appears to be dominated by surface fluxes. Cooling on day -12 is accompanied by negative flux anomalies, while warming on days -6 and 0 coincides with positive fluxes. Finally, the off-equatorial cooling observed on day +12, primarily in the western basin, is consistent with negative surface flux anomalies.

https://doi.org/10.5194/egusphere-2026-4587
Preprint. Discussion started: 3 August 2026

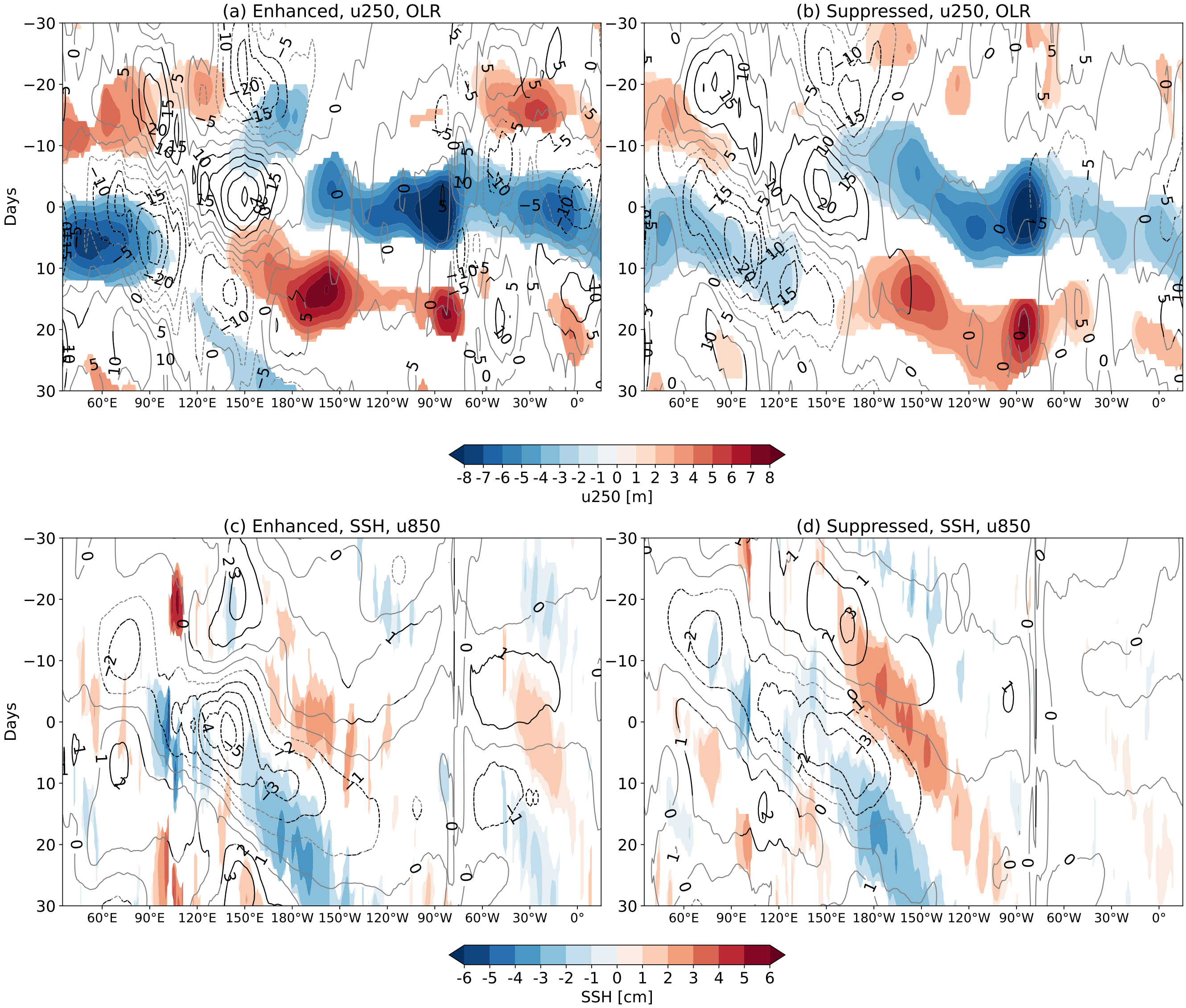

Figure 13. Hovmöller diagrams of lead–lag days for the same MJO events as in Figure 10 averaged between 2°S and 2°N, for anomalies of different variables: (a) u250 (shading in ms^{-1}) and OLR (contours, from -30 Wm^{-2} to 30 Wm^{-2} in increments of 5 Wm^{-2}) during enhanced KW activity in the Atlantic ocena; (b) same as (a) but for suppressed KW activity in the Atlantic ocean. (c) SSH (shading in cm) and u850 (contours, from -5 to 5 ms^{-1} in increments of 1 ms^{-1}) during enhanced KW activity in the Atlantic ocean; (d) same as (c) but for suppressed KW activity in the Atlantic ocean. Shaded regions represent only statistically significant anomalies at the 95 % confidence level, while contour lines are shown in gray for non-significant values and in black for significant values; dashed contours indicate negative values, whereas solid contours denote positive values.

https://doi.org/10.5194/egusphere-2026-4587
Preprint. Discussion started: 3 August 2026

We now turn our attention to the circumglobal characteristics of the MJO that modulate oceanic conditions in the Atlantic. Following our examination of the local ocean–atmosphere forcings associated with individual MJO events, we now proceed to investigate their large-scale global behavior. This allows us to assess how these events evolve prior to reaching the Atlantic and how they subsequently trigger their response within the Atlantic region. Figure 13a–b display lead–lag Hovmöller diagrams of OLR and u250, averaged between 15°N and 15°S, for the enhanced and suppressed cases, respectively. In the enhanced KW activity scenario, there is a convective signal marked by negative OLR anomalies peaking at lag -20 days at 150ºE (Figure 13a). These convective anomalies are associated with the initiation of an eastward-propagating atmospheric KW that can be identified as an easterly wind anomaly between 120°E and 180°E, at lags from -15 to -30 days (Figure 13a). The zonal tropospheric wind anomalies (shaded) depict a clear atmospheric KW pattern that propagates across the Pacific and into the Atlantic, reaching 60ºW after lag -10 days. The wave maintains its structure even in the absence of sustained convection. These upper-level easterly anomalies, together with the lower-level westerly anomalies (Fig. 13c) associated to the atmospheric KW propagation favour the convection observed at 60°W during lags -10 to 0. To further investigate the potential differences between MJO events associated with enhanced or suppressed KW activity in the Atlantic basin, we focus on the equatorial region. Figure 13c–d display Hovmöller diagrams of SSH and u850 corresponding to the enhanced and suppressed cases, respectively. When MJO events are associated with enhanced KW activity in the Atlantic basin, westerly winds of approximately 1 ms^{-1} emerge at 60ºW from day -10, and extend westward to 10ºW. These wind anomalies induce a clearly defined downwelling KW in the Atlantic consistent with the pattern shown in Figure 10a and are coherent with preceding surface wind anomalies over the Pacific, indicating their generation by the atmospheric KW originating from the Maritime Continent during lags -30 to -15, as shown in Figure 13a. Later on, by day 10, a negative low-level wind anomaly of -1 ms^{-1} develops at 60ºW, extending to 40ºW, generating an upwelling KW. Once again, these anomalous low-level wind anomalies exhibit the same sign as anomalies observed in the Pacific basin during preceding days and are triggered by an atmospheric KW at 150°E during lags -10 to +5 that can be tracked in Figure 13a, giving rise to easterly winds. These low-level wind anomalies in the Pacific seem to give rise to SSH anomalies in that basin, which also propagate eastward and exhibit characteristics of oceanic KWs, although they are more diffuse, particularly the downwelling KW.

Conversely, the u250 anomalies presented in Figure 13b indicate an atmospheric KW signal propagating eastward. However, the amplitude and propagation speed of the wave over the Atlantic are reduced compared to what is observed for the oceanic KW enhanced case. In addition, convection at 60°W during lags -10 to 0 and preceding convection at 150°E during lags -30 to -15 are substantially more pronounced in the enhanced than in the suppressed KW activity case. In particular, the convective anomaly around 150°E at lag -20, which appears to initiate the atmospheric KW that subsequently reaches the Atlantic after lag -10, is stronger in the enhanced case, suggesting that the MJO capable of triggering oceanic KWs in the Atlantic is more intense. Next, low-level wind anomalies depicted in Figure 13d and related to the suppressed KW case are not significant over the Atlantic, and only a weak SSH signal can be observed east of 40ºW from approximately day -10 onwards (Figure 13d). In the Pacific basin, east of 150ºE, westerly winds of up to 3 ms^{-1} appear around day -15, followed by easterly winds reaching -3 ms^{-1} near day 5. These wind anomalies give rise to upwelling and downwelling oceanic KWs in the Pacific, respectively.

https://doi.org/10.5194/egusphere-2026-4587
Preprint. Discussion started: 3 August 2026

Finally, the wind anomalies over the eastern and central Atlantic in Figure 13c-d may be associated with the atmospheric KW that originated approximately 20 days earlier over the Indian and Pacific oceans, as seen in Figure 13a-b.

As a summary, we can highlight that over the Atlantic basin, the interaction between MJO and oceanic KWs is weaker than in the other two basins. We find that certain MJO events are capable of triggering KWs over the Atlantic. The link is stronger for MJO phases 3 and 6-7, when low-level westerlies and easterlies, respectively, reach the Atlantic basin. Regarding the former, the strong westerly winds off Brazil, which are related to negative OLR anomalies aloft, trigger downwelling KWs along the equator, which is evidenced both in positive SSH anomalies and positive potential temperature anomalies at the depth of the the thermocline. These waves propagate eastward accros the Atlantic basin, modulating changes in SSTs through modifications of ocean currents and surface temperature horizontal advection. The role of surface heat fluxes seems secondary in explaining the equatorial SST changes. Approximately 20 days before the triggering of the Atlantic KW, the convective activity over the Maritime Continent is enhanced, generating an eastward-propagating atmospheric KW that, later on, acts as a trigger for the Atlantic enhanced convection and surface westerlies. Conversely, those MJO events not associated with oceanic KW in the Atlantic are characterized by weaker wind anomalies at the surface and aloft, and overall weaker equatorial convection over Brazil and West Africa. They, thus, generate minimal SSH response, and the anomalies in the tendency of SST seems to be largely driven by local surface heat fluxes rather than ocean currents. The MJOs preceding these events are more canonical than in the enhanced KW case, but exhibit fainter convective anomalies over the Indo-Pacific, producing less pronounced atmospheric KWs, which likely contribute to the diminished oceanic response in the Atlantic.

5 Discussion and conclusions

The MJO induces a coherent atmospheric response characterized by organized anomalies in convection and low-level zonal wind. Even when analysed on its own (Fig. 2), it leaves a clear but basin-dependent imprint on the upper ocean. Over the Indian ocean, the alternation between enhanced and suppressed convection produces SSH anomalies consistent with the excitation of equatorial Rossby waves, reflecting the complex interaction between wind forcing, reflection, and resonant basin modes. In the western Pacific, strong westerly and easterly wind anomalies associated with successive MJO phases efficiently force downwelling and upwelling equatorial KWs that propagate eastward, although their amplitude weakens as they approach the central Pacific. By contrast, the oceanic response in the eastern Pacific and in the Atlantic remains weak, indicating that the atmospheric signature of the MJO does not translate uniformly into equatorial wave activity. Thus, although the phase-based composite suggests a potential interaction with oceanic KWs in the three basins, it neither quantifies this interaction nor distinguishes the MJO events that produce it from those that do not.

A complementary view emerges from analysing KWs independently in each basin. In the Indian ocean, the SSH signal moves eastward and includes strong off-equatorial features, with u850 anomalies confined to the central sector that reverse sign in phase with the SSH pattern. In the Pacific, the KW index captures a well-defined downwelling signal that originates with westerly winds in the west and retains a typical KW shape as it propagates eastward without additional forcing, whereas in the Atlantic even weak wind anomalies generate an SSH signal that progresses from west to east. Across all three basins,

https://doi.org/10.5194/egusphere-2026-4587
Preprint. Discussion started: 3 August 2026

the sign of u850 systematically corresponds to the nature of the SSH response, with downwelling and upwelling phases linked to westerly and easterly anomalous wind conditions, respectively.

However, neither of the two previous approaches allows us to determine what fraction of MJO events trigger equatorial KWs, what their main characteristics are, or how these propagating waves may later feed back on surface properties such as SST. To answer these questions, we developed a methodology based on matching MJO days with periods of KW activity in each of the three ocean basins, each characterized by its own independently derived KW index, and classified MJO events into two categories: those exhibiting enhanced KW activity and those associated with suppressed KW activity. Despite limitations arising from the 20-to-90-day band-pass filter, which may exclude variability outside this temporal range, and from differences in the number of significant KW entries across basins in the contingency tables, this framework provides a consistent basis for examining how varying levels of oceanic KW activity relate to the evolution of MJO events.

Between 38.4% and 58.4% of MJO events generate KWs in the Pacific. These events feature stronger and more zonally coherent wind and convective anomalies, in agreement with previous studies showing that the efficiency of KW excitation depends strongly on the zonal fetch and coherence of intraseasonal wind forcing (Kessler et al., 1995; Seo and Xue, 2005). Conversely, between 51.1% and 77.6% of oceanic KWs in the Pacific are associated with the MJO, and their presence supports its eastward advance by maintaining subsurface adjustments that sustain SST anomalies even where atmospheric forcing weakens; in their absence, SST variability depends mainly on surface fluxes in the central basin and on local processes such as surface current convergence in the east. Taken together, these results indicate that intraseasonal SST changes in the Pacific are driven by MJO convection and associated radiative heat fluxes in the western basin, by KW-induced zonal and vertical temperature advection in the central basin, and by turbulent fluxes and horizontal advection in the east.

In the Indian ocean, between 16.8% and 62% of MJO events give rise to oceanic KWs, indicating a weaker interaction than in the Pacific. KW generation is favored by coherent westerly wind anomalies over the central basin, identified in previous studies as the key driver of intraseasonal oceanic wave responses (Han, 2005; Moum et al., 2016), and the resulting SSH signal follows the canonical KW response to MJO forcing described by Webber et al. (2010). When forcing is weak or displaced off the equator, no clear equatorial wave develops, in line with Han (2005). In turn, between 17.4% and 64.2% of oceanic KWs are associated with the MJO, but — in contrast with the Pacific — their presence modulates rather than controls its eastward propagation: OLR anomalies can still cross the basin without KWs, although with reduced amplitude and weaker ocean–atmosphere coupling and SST variability is then primarily governed by surface heat fluxes.

In the Atlantic, between 9.4% and 57.9% of MJO events give rise to oceanic KWs, although the contingency table contains fewer significant entries than in the other basins and the MJO wind signature is confined to a few phases, so these estimates should be interpreted with caution. KW generation requires coherent westerly wind stress anomalies near the South American coast and is favored by an atmospheric KW originating over the Indo-Pacific that remains coherent upon entering the basin and promotes convection near 60°W, consistent with previous evidence of KW activity extending into the Atlantic (Roundy and Kiladis, 2006); otherwise, convective anomalies remain concentrated over the eastern basin and the Guinea Dome, decoupled from the equatorial ocean. In turn, between 10.4% and 64.6% of oceanic KWs are linked to the MJO, and their presence enhances coupling from the western to the central basin by allowing subsurface signals to propagate independently of local

https://doi.org/10.5194/egusphere-2026-4587
Preprint. Discussion started: 3 August 2026

forcing. As in the Pacific, SST tendencies under active KW conditions are dominated by ocean dynamics, with current-induced advection gaining importance in the east, whereas without KWs they are largely controlled by surface heat fluxes.

The vertical profiles associated with KW propagation along the equator (Figs. 5, 9 and 11) reveal an inclination in the anomalous signal comparable to that recently identified by Robbins et al. (2025), who attribute it to the vertical propagation of the surface-forced signal and note that the shadow zone in the western basin and reflections in the east give rise to highly heterogeneous propagation along the equatorial path. Our results extend this argument by showing that climatological factors also play a role: the thermocline, deeper in the western Atlantic and Pacific and in the eastern Indian ocean, and shallower in the opposite portions of each basin, increases the phase speed of KWs and concentrates most of the energy in the lower modes where it is deep and in the higher modes where it is shallow. Additional climatological features, notably the background velocity field associated with the Equatorial Undercurrent (EUC), may likewise shape the representation of the signal along the propagation path.

A further question is the extent to which the representation of KW forcing conditions that of the MJO itself. Part of the answer lies in the surface–subsurface oceanic relationship, which differs markedly across basins. In the Pacific, the KW signal exhibits high coherence, particularly in the central basin, with a temporal lag of approximately 15 days (not shown); this lag varies along the path as the thermocline shoals eastward and reduces the phase speed of the KW, while other SST drivers, such as turbulent and radiative fluxes, become active in different sections of the trajectory. In the Atlantic, the coherence between surface temperature and the thermocline is nearly simultaneous, which may reflect both the shape of the thermocline and the relatively small size of the basin. The Indian ocean behaves differently: although the basin is comparatively small, the thermocline deepens toward its eastern portion, with a minimum depth near 60°E, accelerating horizontal propagation and intensifying the signal near the coast of Sumatra. There, surface and subsurface temperatures are in phase opposition — the surface responds to changes in OLR whereas the thermocline temperature responds to equatorial winds — so that the surface–thermocline coherence is consistently negative, with a phase lag of approximately 20 days (not shown), and SST is predominantly controlled by radiative fluxes.

These findings show that each ocean basin exhibits distinct characteristics with respect to MJO propagation in the form of KWs and its impact on SST, underscoring the need to analyse each basin separately in order to understand its relationship with the MJO unequivocally.

Collectively, the results suggest that numerical models must adequately represent both the equatorial winds associated with the MJO and the vertical structure of the thermocline in each basin in order to capture the ocean–atmosphere coupling associated with this system, a requirement that is particularly relevant for subseasonal-to-seasonal prediction. Improving the simulation of equatorial wave dynamics and their interaction with atmospheric convection remains essential for capturing the eastward propagation and predictability of the MJO (Wheeler and Hendon, 2004; Kim et al., 2014), while coupled models must also accurately represent subsurface processes, including thermocline adjustments and their feedback on SST, which have been shown to enhance MJO skill beyond atmosphere-only frameworks (DeMott et al., 2015). The basin-dependent behaviour identified here further implies that regional biases in wind stress and stratification can significantly affect forecast skill; advancing subseasonal-to-seasonal prediction may therefore require higher vertical resolution in the ocean component

https://doi.org/10.5194/egusphere-2026-4587
Preprint. Discussion started: 3 August 2026

and coupling strategies that capture the timing and structure of KW-related signals. Finally, the vertical propagation of these KW signals into the thermocline raises the question of their possible contribution to ocean mixing processes, which warrants further analysis.

Code and data availability. Data used in this work are publicly available from the ERA5 reanalysis (https://cds.climate.copernicus.eu/datasets/reanalysis-era5-single-levels?tab=overview) and from the Copernicus Marine Environment Monitoring Service (CMEMS) ocean re-analysis, specifically the GLORYS12V1 product (https://data.marine.copernicus.eu/product/GLOBAL_MULTIYEAR_PHY_001_030/description). The original data were processed using Climate Data Operators (CDO; Schulzweida, 2023) and custom Python scripts. The scripts used in this study are available from the corresponding author upon reasonable request.

Author contributions. EM, IP, and FB conceived the methodology. FB performed the formal analysis, with support from IP and EM, and wrote the original draft. All authors reviewed and edited the manuscript.

Competing interests. Authors declare no competing interests.

Acknowledgements. This manuscript received funding from the Spanish Ministry of Science and Innovation from SIWA project (grant no. PID2025-168561NB-I00).

https://doi.org/10.5194/egusphere-2026-4587
Preprint. Discussion started: 3 August 2026

References

Alaka, G. J. and Maloney, E. D.: The Influence of the MJO on Upstream Precursors to African Easterly Waves, Journal of Climate, 25, 3219 – 3236, https://doi.org/10.1175/JCLI-D-11-00232.1, 2012.

Alvarez, M. S., Vera, C. S., Kiladis, G. N., and Liebmann, B.: Influence of the Madden Julian Oscillation on precipitation and surface air temperature in South America, Climate Dynamics, 46, 245–262, https://doi.org/10.1007/s00382-015-2581-6, 2016.

Butterworth, S.: On the Theory of Filter Amplifiers, Experimental Wireless & the Wireless Engineer, 7, 536–541, 1930.

Carvalho, L. M. V., Jones, C., and Liebmann, B.: The South Atlantic Convergence Zone: Intensity, Form, Persistence, and Relationships with Intraseasonal to Interannual Activity and Extreme Rainfall, Journal of Climate, 17, 88 – 108, https://doi.org/10.1175/1520-0442(2004)017<0088:TSACZI>2.0.CO;2, 2004.

Cassou, C.: Intraseasonal interaction between the Madden–Julian Oscillation and the North Atlantic Oscillation, Nature, 455, 523–527, https://doi.org/10.1038/nature07286, 2008.

DeMott, C. A., Klingaman, N. P., and Woolnough, S. J.: Atmosphere-ocean coupled processes in the Madden-Julian oscillation, Reviews of Geophysics, 53, 1099–1154, https://doi.org/10.1002/2014RG000478, 2015.

Diakhaté, M., de Coëtlogon, G., Lazar, A., Wade, M., and Gaye, A. T.: Intraseasonal variability of tropical Atlantic sea-surface temperature: air–sea interaction over upwelling fronts, Quarterly Journal of the Royal Meteorological Society, 142, 372–386, https://doi.org/https://doi.org/10.1002/qj.2657, 2016.

Drushka, K., Sprintall, J., and Gille, S. T.: Subseasonal variations in salinity and barrier-layer thickness in the eastern equatorial Indian Ocean, Journal of Geophysical Research: Oceans, 119, 805–823, https://doi.org/https://doi.org/10.1002/2013JC009422, 2014.

Fedorov, A. V. and Brown, J. N.: Equatorial Waves, in: Encyclopedia of Ocean Sciences, vol. 2, pp. 100–110, Academic Press, San Diego, 2009.

Gorgas García, F. J., Cardiel López, N., and Zamorano Calvo, J.: Contraste de la independencia de caracteres, in: Estadística básica para estudiantes de ciencias, pp. 167–169, Universidad Complutense de Madrid, España, ISBN 978-84-691-8981-8, 2011.

Grimm, A. M.: Madden–Julian Oscillation impacts on South American summer monsoon season: precipitation anomalies, extreme events, teleconnections, and role in the MJO cycle, Climate Dynamics, 53, 907–932, https://doi.org/10.1007/s00382-019-04622-6, 2019.

Han, W.: Origins and Dynamics of the 90-Day and 30–60-Day Variations in the Equatorial Indian Ocean, Journal of Physical Oceanography, 35, 708 – 728, https://doi.org/10.1175/JPO2725.1, 2005.

Hendon, H. H., Zhang, C., and Glick, J. D.: Interannual Variation of the Madden–Julian Oscillation during Austral Summer, Journal of Climate, 12, 2538 – 2550, https://doi.org/10.1175/1520-0442(1999)012<2538:IVOTMJ>2.0.CO;2, 1999.

Janicot, S., Caniaux, G., Chauvin, F., de Coëtlogon, G., Fontaine, B., Hall, N., Kiladis, G., Lafore, J.-P., Lavaysse, C., Lavender, S. L., Leroux, S., Marteau, R., Mounier, F., Philippon, N., Roehrig, R., Sultan, B., and Taylor, C. M.: Intraseasonal variability of the West African monsoon, Atmospheric Science Letters, 12, 58–66, https://doi.org/https://doi.org/10.1002/asl.280, 2011.

Kalnay, E., Kanamitsu, M., Kistler, R., Collins, W., Deaven, D., Gandin, L., Iredell, M., Saha, S., White, G., Woollen, J., Zhu, Y., Chelliah, M., Ebisuzaki, W., Higgins, W., Janowiak, J., Mo, K. C., Ropelewski, C., Wang, J., Leetmaa, A., and ... Joseph, D.: The NCEP/NCAR 40-Year Reanalysis Project, Bulletin of the American Meteorological Society, 77, 437–471, https://doi.org/10.1175/1520-0477(1996)077<0437:TNYRP>2.0.CO;2, 1996.

Kessler, W. S., McPhaden, M. J., and Weickmann, K. M.: Forcing of intraseasonal Kelvin waves in the equatorial Pacific, Journal of Geophysical Research: Oceans, 100, 10 613–10 631, https://doi.org/https://doi.org/10.1029/95JC00382, 1995.

https://doi.org/10.5194/egusphere-2026-4587
Preprint. Discussion started: 3 August 2026

Kim, D., Xavier, P., Maloney, E., Wheeler, M., Waliser, D., Sperber, K., Hendon, H., Zhang, C., Neale, R., Hwang, Y.-T., and Liu, H.: Process-Oriented MJO Simulation Diagnostic: Moisture Sensitivity of Simulated Convection, Journal of Climate, 27, 5379 – 5395, https://doi.org/10.1175/JCLI-D-13-00497.1, 2014.

Kim, H.-M., Kim, D., Vitart, F., Toma, V. E., Kug, J.-S., and Webster, P. J.: MJO Propagation across the Maritime Continent in the ECMWF Ensemble Prediction System, Journal of Climate, 29, 3973 – 3988, https://doi.org/10.1175/JCLI-D-15-0862.1, 2016.

Klingaman, N. P. and Woolnough, S. J.: The role of air–sea coupling in the simulation of the Madden–Julian oscillation in the Hadley Centre model, Quarterly Journal of the Royal Meteorological Society, 140, 2272–2286, https://doi.org/https://doi.org/10.1002/qj.2295, 2014.

Lafleur, D. M., Barrett, B. S., and Henderson, G. R.: Some Climatological Aspects of the Madden–Julian Oscillation (MJO), Journal of Climate, 28, 6039–6053, https://doi.org/10.1175/JCLI-D-14-00744.1, 2015.

Lee, R. W., Woolnough, S. J., Charlton-Perez, A. J., and Vitart, F.: ENSO Modulation of MJO Teleconnections to the North Atlantic and Europe, Geophysical Research Letters, 46, 13 535–13 545, https://doi.org/https://doi.org/10.1029/2019GL084683, 2019.

Lee, S.-K., Lopez, H., Tuchen, F. P., Kim, D., Foltz, G. R., and Wittenberg, A. T.: On the Genesis of the 2021 Atlantic Niño, Geophysical Research Letters, 50, e2023GL104 452, https://doi.org/https://doi.org/10.1029/2023GL104452, e2023GL104452 2023GL104452, 2023.

Lellouche, J.-M., Greiner, E., Bourdallé-Badie, R., Garric, G., Melet, A., Drévillon, M., Bricaud, C., Hamon, M., Le Galloudec, O., Regnier, C., Candela, T., Testut, C.-E., Gasparin, F., Ruggiero, G., Benkiran, M., Drillet, Y., and Le Traon, P.-Y.: The Copernicus Global 1/12° Oceanic and Sea Ice GLORYS12 Reanalysis, Frontiers in Earth Science, 9, 698 876, https://doi.org/10.3389/feart.2021.698876, 2021.

Liang, Y.-C. and Fedorov, A. V.: Linking the Madden–Julian Oscillation, tropical cyclones and westerly wind bursts as part of El Niño development, Climate Dynamics, 57, 1039–1060, https://doi.org/10.1007/s00382-021-05757-1, 2021.

Lin, H., Brunet, G., and Derome, J.: An Observed Connection between the North Atlantic Oscillation and the Madden–Julian Oscillation, Journal of Climate, 22, 364 – 380, https://doi.org/10.1175/2008JCLI2515.1, 2009.

Liu, L., Li, Y., and Wang, F.: MJO-Induced Intraseasonal Mixed Layer Depth Variability in the Equatorial Indian Ocean and Impacts on Subsurface Water Obduction, Journal of Physical Oceanography, 51, 1247 – 1263, https://doi.org/10.1175/JPO-D-20-0179.1, 2021.

Madden, R. A. and Julian, P. R.: Detection of a 40–50 Day Oscillation in the Zonal Wind in the Tropical Pacific, Journal of Atmospheric Sciences, 28, 702 – 708, https://doi.org/10.1175/1520-0469(1971)028<0702:DOADOI>2.0.CO;2, 1971.

Madden, R. A. and Julian, P. R.: Description of Global-Scale Circulation Cells in the Tropics with a 40–50 Day Period, Journal of Atmospheric Sciences, 29, 1109 – 1123, https://doi.org/10.1175/1520-0469(1972)029<1109:DOGSCC>2.0.CO;2, 1972.

Matsuno, T.: Quasi-Geostrophic Motions in the Equatorial Area, Journal of the Meteorological Society of Japan. Ser. II, 44, 25–43, https://doi.org/10.2151/jmsj1965.44.1_25, 1966.

Matthews, A. J. and Kiladis, G. N.: The Tropical–Extratropical Interaction between High-Frequency Transients and the Madden–Julian Oscillation, Monthly Weather Review, 127, 661 – 677, https://doi.org/10.1175/1520-0493(1999)127<0661:TTEIBH>2.0.CO;2, 1999.

Matthews, A. J., Singhruck, P., and Heywood, K. J.: Ocean Temperature and Salinity Components of the Madden–Julian Oscillation Observed by Argo Floats, Climate Dynamics, 35, 1149–1168, https://doi.org/10.1007/s00382-009-0631-7, 2010.

Mayta, V. C., Ambrizzi, T., Carlo Espinoza, J., and Silva Dias, P. L.: The role of the Madden-Julian oscillation on the Amazon Basin intraseasonal rainfall variability, INTERNATIONAL JOURNAL OF CLIMATOLOGY, 39, 343–360, https://doi.org/10.1002/joc.5810, 2019.

McPhaden, M. J. and Yu, X.: Equatorial waves and the 1997–98 El Niño, Geophysical Research Letters, 26, 2961–2964, https://doi.org/https://doi.org/10.1029/1999GL004901, 1999.

https://doi.org/10.5194/egusphere-2026-4587
Preprint. Discussion started: 3 August 2026

Moum, J. N., Pujiana, K., Lien, R.-C., and Smyth, W. D.: Ocean feedback to pulses of the Madden–Julian Oscillation in the equatorial Indian Ocean, Nature Communications, 7, 13 203, https://doi.org/10.1038/ncomms13203, 2016.

Robbins, C., Matthews, A. J., Hall, R. A., Webber, B. G. M., and Heywood, K. J.: The Equatorial Deep Ocean Structure Associated With the Madden-Julian Oscillation From an Ocean Reanalysis, Journal of Geophysical Research: Oceans, 130, e2025JC022 457, https://doi.org/https://doi.org/10.1029/2025JC022457, e2025JC022457 2025JC022457, 2025.

Roundy, P. E. and Kiladis, G. N.: Observations of convectively coupled Kelvin waves in the Eastern Pacific and Atlantic Oceans, Journal of Climate, 19, 4034–4047, https://doi.org/10.1175/JCLI3831.1, 2006.

Rydbeck, A. V., Jensen, T. G., and Flatau, M.: Characterization of Intraseasonal Kelvin Waves in the Equatorial Pacific Ocean, Journal of Geophysical Research: Oceans, 124, 2028–2053, https://doi.org/https://doi.org/10.1029/2018JC014838, 2019.

Rydbeck, A. V., Jensen, T. G., and Flatau, M. K.: Reciprocity in the Indian Ocean: Intraseasonal Oscillation and Ocean Planetary Waves, Journal of Geophysical Research: Oceans, 126, e2021JC017 546, https://doi.org/https://doi.org/10.1029/2021JC017546, e2021JC017546 2021JC017546, 2021.

Seo, K.-H. and Son, S.-W.: The Global Atmospheric Circulation Response to Tropical Diabatic Heating Associated with the Madden–Julian Oscillation during Northern Winter, Journal of the Atmospheric Sciences, 69, 79 – 96, https://doi.org/10.1175/2011JAS3686.1, 2012.

Seo, K.-H. and Xue, Y.: MJO-related oceanic Kelvin waves and the ENSO cycle: A study with the NCEP Global Ocean Data Assimilation System, Geophysical Research Letters, 32, https://doi.org/https://doi.org/10.1029/2005GL022511, 2005.

Slingo, J. M., Rowell, D. P., Sperber, K. R., and Nortley, F.: On the predictability of the interannual behaviour of the Madden-Julian oscillation and its relationship with el Niño, Quarterly Journal of the Royal Meteorological Society, 125, 583–609, https://doi.org/https://doi.org/10.1002/qj.49712555411, 1999.

Soci, C., Hersbach, H., Simmons, A., Poli, P., Bell, B., Berrisford, P., Horányi, A., Muñoz-Sabater, J., Nicolas, J., Radu, R., Schepers, D., Villaume, S., Haimberger, L., Woollen, J., Buontempo, C., and Thépaut, J.-N.: The ERA5 global reanalysis from 1940 to 2022, Quarterly Journal of the Royal Meteorological Society, 150, 4014–4048, https://doi.org/10.1002/qj.4803, 2024.

Ventrice, M. J., Thorncroft, C. D., and Roundy, P. E.: The Madden–Julian Oscillation's Influence on African Easterly Waves and Downstream Tropical Cyclogenesis, Monthly Weather Review, 139, 2704 – 2722, https://doi.org/10.1175/MWR-D-10-05028.1, 2011.

Vera, C. S., Alvarez, M. S., Gonzalez, P. L. M., Liebmann, B., and Kiladis, G. N.: Seasonal cycle of precipitation variability in South America on intraseasonal timescales, Climate Dynamics, 51, 1991–2001, https://doi.org/10.1007/s00382-017-3994-1, 2018.

Vitart, F. and Molteni, F.: Simulation of the Madden– Julian Oscillation and its teleconnections in the ECMWF forecast system, Quarterly Journal of the Royal Meteorological Society, 136, 842–855, https://doi.org/https://doi.org/10.1002/qj.623, 2010.

Wang, W., Hung, M.-P., Weaver, S. J., Kumar, A., and Long, L. N.: MJO prediction in the NCEP Climate Forecast System version 2, Climate Dynamics, 42, 2509–2520, https://doi.org/10.1007/s00382-013-1806-9, 2014.

Webber, B. G. M., Matthews, A. J., and Heywood, K. J.: A dynamical ocean feedback mechanism for the Madden–Julian Oscillation, Quarterly Journal of the Royal Meteorological Society, 136, 740–754, https://doi.org/https://doi.org/10.1002/qj.604, 2010.

Webber, B. G. M., Matthews, A. J., Heywood, K. J., Kaiser, J., and Schmidtko, S.: Seaglider observations of equatorial Indian Ocean Rossby waves associated with the Madden–Julian Oscillation, Journal of Geophysical Research: Oceans, 119, 3714–3731, https://doi.org/10.1002/2013JC009657, 2014.

Wheeler, M. C. and Hendon, H. H.: An All-Season Real-Time Multivariate MJO Index: Development of an Index for Monitoring and Prediction, Monthly Weather Review, 132, 1917 – 1932, https://doi.org/10.1175/1520-0493(2004)132<1917:AARMMI>2.0.CO;2, 2004.

https://doi.org/10.5194/egusphere-2026-4587
Preprint. Discussion started: 3 August 2026

Zhang, C.: Madden–Julian Oscillation: Bridging Weather and Climate, Bulletin of the American Meteorological Society, 94, 1849 – 1870, https://doi.org/10.1175/BAMS-D-12-00026.1, 2013.

Zhang, C. and Dong, M.: Seasonality in the Madden–Julian Oscillation, Journal of Climate, 17, 3169 – 3180, https://doi.org/10.1175/1520-0442(2004)017<3169:SITMO>2.0.CO;2, 2004.

Zhang, C. and Gottschalck, J.: SST Anomalies of ENSO and the Madden–Julian Oscillation in the Equatorial Pacific, Journal of Climate, 15, 2429 – 2445, https://doi.org/10.1175/1520-0442(2002)015<2429:SAOEAT>2.0.CO;2, 2002.

Zhou, S. and Miller, A. J.: The Interaction of the Madden–Julian Oscillation and the Arctic Oscillation, Journal of Climate, 18, 143 – 159, https://doi.org/10.1175/JCLI3251.1, 2005.